Nucleic Acids Research, 2025, **53**, gkaf315
https://doi.org/10.1093/nar/gkaf315
Computational Biology

3D genome organization shapes DNA damage susceptibility to platinum-based drugs

Ye Wang[1,2,3], **Asli Yildirim**[1,2], **Lorenzo Boninsegna**[1,2], **Valentina Christian**[3], **Sung-Hae L. Kang**[3], **Xianghong Jasmine Zhou**[1,3,*], **Frank Alber**[1,2,*]

[1]Institute of Quantitative and Computational Biosciences (QCBio), University of California Los Angeles, Los Angeles CA90095, United States
[2]Department of Microbiology, Immunology, and Molecular Genetics, University of California Los Angeles, 520 Boyer Hall, Los Angeles CA90095, United States
[3]Department of Pathology and Laboratory Medicine, David Geffen School of Medicine, University of California Los Angeles, 10833 Le Conte Ave, Los Angeles CA90095, United States

[*]To whom correspondence should be addressed. Email: falber@g.ucla.edu
Correspondence may also be addressed to Xianghong Jasmine Zhou. Email: XJZhou@mednet.ucla.edu

Abstract

Platinum (Pt) drugs are widely utilized in cancer chemotherapy. Although cytotoxic and resistance mechanisms of Pt drugs have been thoroughly explored, it remains elusive what factors affect the receptiveness of DNA to drug-induced damage in nuclei. Here, we demonstrate that nuclear locations of chromatin play a key role in Pt drug-induced DNA damage susceptibility *in vivo*. By integrating data from damage-seq experiments with 3D genome structure information, we show that nuclear locations of chromatin relative to specific nuclear bodies and compartments explain patterns of cisplatin DNA damage susceptibility. This aligns with observations of cisplatin enrichment in biomolecular condensates at certain nuclear bodies. Finally, 3D structure mapping of DNA damage reveals characteristic differences between nuclear distributions of oxaliplatin-induced DNA damage in drug resistant versus sensitive cells. DNA damage increases in gene-poor chromatin at the nuclear periphery, while it decreases in gene-rich regions located at nuclear speckles. This suggests a strategic redistribution of Pt drug-induced damage in nuclei during chemoresistance development.

Graphical abstract

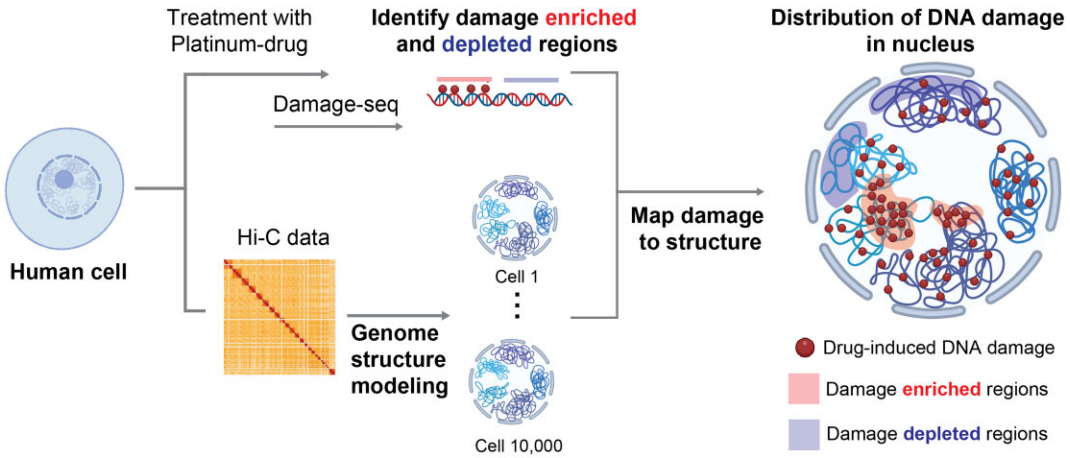

Introduction

Platinum drugs (Pt drugs), such as cisplatin, oxaliplatin, and carboplatin, are major front-line anti-cancer treatments widely used for various cancers, including lung cancer, ovarian cancer, colon cancer, head and neck cancer, breast cancer, and brain cancer [1–3]. However, the almost inevitable relapse of cancer following Pt drug treatment remains a major challenge [2, 3]. Gaining a better understanding of cellular response processes to Pt drug treatment is key for designing strategies to increase Pt drug cytotoxicity and overcome resistance.

Two recently developed methods, damage-seq [4] and cisplatin-seq [5], have mapped the locations of Pt drug–DNA adducts in the genome at single-base-pair resolution. In damage-seq an antibody specific to Pt drug–DNA adducts

Received: June 25, 2024. **Revised:** March 31, 2025. **Editorial Decision:** April 1, 2025. **Accepted:** May 23, 2025

is used for immunoprecipitation of drug-damaged DNA, followed by massively parallel sequencing to identify the locations of damaged DNA sites. In cisplatin-seq, a recombinant HMGB1 protein recognizes Pt-drug induced DNA distortions at damage sites. Both studies indicated that the local chromatin structure influences the distribution of cisplatin-induced damage in the genome [4, 5]. For instance, damage-seq revealed a slight decrease in cisplatin-induced damage at the location of nucleosomes in the DNA sequence. Moreover, inhibitors of chromatin remodeling complexes that promote chromatin compaction (e.g. histone deactetylases and DNA methyltransferases) have been shown to increase the cytotoxicity of Pt drugs and even overcome resistance in lung cancer, pointing to a role of local chromatin structure in the cisplatin-based cancer therapy [6–12]. Additionally, imaging experiments revealed that Pt drug concentrations are depleted in heterochromatic regions [13].

However, local chromatin condensation is not the only factor influencing the susceptibility of specific DNA regions to Pt drug-induced DNA damage. Recent imaging studies have shown increased colocalization of Pt drugs with several nuclear bodies, including transcriptional condensates, nuclear speckles, and nucleoli, pointing to an increased concentration of Pt drugs in specific biomolecular condensates [8, 14, 15]. These studies therefore suggest that the sub-nuclear location of chromatin regions can expose certain DNA regions associated with nuclear bodies to higher local concentrations of Pt drugs, leading to a higher overall susceptibility of these regions to DNA damage. Moreover, Pt drug treatment has been shown to trigger nucleolar stress and aberrant nucleolar morphology [16–18].

Despite these advances, it remains unclear how the nuclear architecture influences Pt drug distributions *in vivo*, and if uneven Pt drug distributions could explain variations in DNA damage susceptibility across genomic regions. Imaging and genomics studies have shown that chromosomes occupy distinct territories within the nucleus, with preferred spatial locations [19]. For example, some chromosomal regions, mostly transcriptionally active, are preferentially located toward the nuclear interior, whereas others, mostly silenced regions, show high probability to occupy the nuclear periphery near the nuclear lamina. Certain chromosomal regions were found with higher propensity close to nuclear speckles, while others show preferential locations toward nucleoli, the lamina compartment or other nuclear bodies [19, 20]. The preferential locations of genomic regions can vary between cell types and during cell differentiation [20]. Thus, uneven distributions of Pt-drugs in the nuclear environment may expose chromatin regions to different levels of DNA damage susceptibility depending on their preferential location in the nucleus. However, no study exists today that has explored in detail the role of the 3D nuclear architecture in the distribution of Pt drug-induced DNA damage on a genome-wide scale. Moreover, it remains unclear whether manipulation of this uneven distribution of Pt-drug induced DNA damage could contribute to the development of cancer-resistant cell.

Here, we fill this gap. In this work, we aim to study the relationship between the 3D nuclear locations of chromosomal regions and their susceptibility to cisplatin and oxaliplatin drug induced DNA damages. We previously developed a population-based genome structure modeling approach, which uses Hi-C data [21, 22] to generate a population of single-cell 3D genome structures that not only recapitulate the Hi-C data but also accurately predict orthogonal experimental data describing the nuclear organization of genomic regions [22, 23], including their average radial positions from GPSeq experiments [24], distances to nuclear speckles from SON-TSA-seq data [25], and nuclear lamina from lamin B1 TSA-seq and DamID data [25, 26], as well as single-cell chromosome conformations from multiplex DNA-FISH imaging [27]. Here, we use such 3D genome structures (see Materials and methods) to explore the distribution of cisplatin- and oxaliplatin-induced DNA damage throughout the 3D nuclear genome organization using damage-seq data. Specifically, we study wether the preferential nuclear locations of genomic regions relative to specific nuclear bodies and compartments influences the distribution of DNA damage susceptibility observed in damage-seq experiments. Our results demonstrate that the global 3D genome structure organization plays a major role in modulating Pt drug-induced DNA damage levels, both for increasing and alleviating cisplatin-induced damage in specific DNA regions. Strikingly, we found that a dominant factor in the enrichment of DNA damage in the nuclear environment is a close distance to nuclear speckles and an interior radial position in the nucleus. We also found that cisplatin drug-induced damage is not only enriched in transcriptionally active regions but also slightly enriched in polycomb-repressed regions of the B1 subcompartment, which can be explained by the location of some polycomb-repressed regions at the nuclear interior close to speckles [28, 29]. Thus, our results demonstrate that DNA damage susceptibility depends not only on the local chromatin structure and DNA accessibility but also on global factors related to the nuclear organization, likely due to enriched concentrations of cisplatin in nuclear bodies and biomolecular condensates at preferential locations in the nucleus. This finding supports recent observations that cisplatin can be enriched in molecular condensates linked to nuclear bodies [14, 15]. To further investigate how nuclear architecture contributes to the development of cancer chemoresistance, we conducted Hi-C and oxaliplatin damage-seq experiments on both chemosensitive and chemoresistant HCT116 cancer cell lines, generating 3D genome structures for both cell lines. A comparative analysis revealed that, in chemoresistant cells, oxaliplatin-induced damage was reduced in gene-rich chromatin adjacent to nuclear speckles, while damage was increased in gene-poor regions associated with nuclear lamina compartment. The altered DNA damage distribution in chemoresistant cells agrees with the classical "bodyguard hypothesis", which suggests that heterochromatin in the lamina compartment acts as a protective buffer for gene-rich euchromatin against DNA damage [30]. Thus, our results underscore the influence of global nuclear organization on DNA damage susceptibility, providing a mechanistic insight relevant for future studies in Pt-drug resistance and cytotoxicity.

Materials and methods

Cell culture

Oxaliplatin sensitive HCT116 cell line (HCT116 OxS cell) is purchased from ATCC (https://www.atcc.org/products/ccl-247); oxaliplatin resistant HCT116 cell line (HCT116 OxR cell) was obtained from MD Anderson Cancer Center Characterized Cell Line Core, supplied and generated by the Dr. Lee Ellis Laboratory. Both HCT116 OxS and HCT116 OxR were

cultured in McCoy's 5A cell culture medium (Gibco) with 10% (v/v) fetal bovine serum (FBS) and 1% (v/v) PenStrep. Cells are grown at 37°C in a humidified 5% CO_2 incubator. Both cells were screened for Mycoplasma contamination with MycoStrip (InvivoGen, rep-mys-10) and tested negative.

Chromosome ploidy and karyotype analysis

Chromosome analysis was performed using standard operating procedures for GTG banded (G-banding with Trypsin and Giemsa staining) karyotype analysis. A total of 20 metaphase cells were fully analyzed to detect chromosomal abnormalities. Ploidy assessment indicated that all examined cells were near-diploid, harboring 44–45 chromosomes, consistent with the parental HCT116 cell line [31, 32]. The composite karyotypic profile of HCT116 OxR broadly resembled that of the parental line, notably exhibiting unbalanced translocations resulting in a derivative chromosome 16 [der(16)t(8;16)(q13;p13) and a derivative chromosome 18 [der(18)t(17;18)(q12;p11.3)], as well as a consistent loss of the Y chromosome. Additional abnormalities unique to HCT116 OxR included a deletion of the short arm of chromosome 1 [del(1)(p12)], the presence of additional unknown chromatin material on the short arm of chromosome 15 [add(15)(p11.2)] observed as a homogeneously staining region, extra chromatin material on the short arm of chromosome 18 [add(18)(p11.1)], and loss of one copy of chromosome 18 in some cells. Moreover, 1–5 double minutes and additional chromatin material on the long arm of chromosome 10 [add(10)(q22)] were noted. Although an abnormality involving chromosome 10 was reported in the parental cell line, it is unclear whether this observation corresponds directly due to the limitations of G-banded karyotyping.

Treatment with oxaliplatin

Cells were cultured until they reached 70% confluency before treatment. In previous cisplatin damage-seq, GM12878 cell line was treated by 200 μM cisplatin for 1.5 h. Oxaliplatin has lower dose of treatment concentration for colon cancer compared to cisplatin due to its higher cytotoxicity (https://www.cancerrxgene.org). To make the oxaliplatin treatment comparable to cisplatin damage-seq, oxaliplatin (Sigma, #O9512) was dissolved in DMF (N,N-Dimethylformamide, D4551, Sigma)to create a 4 mM stock solution, which was then added to the medium to achieve a final concentration of 50 μM. The viability of cells treated with DMF alone (97.2% and 97.6%) is comparable to untreated cells (98.0% and 97.3%), indicating that the concentration of DMF used does not adversely affect cell viability. After added oxaliplatin, cells were further incubated for either 3 or 24 h at incubator. Following incubation, the cells were washed with PBS and collected via trypsin digestion. The resulted cell pellets were then frozen at −80°C. For *in vitro* experiments, 2 μg genomic DNA was treated with 50 μM oxaliplatin in an aqueous solution at 37°C for 15 min. The DNA was then purified using 2× AMPure XP beads (Beckman, #A63881) for damage-seq library preparation.

Oxaliplatin damage-seq

Oxaliplatin damaged-DNA immunoprecipitation

The oxaliplatin damage-seq method is adapted from the protocol described in both cisplatin-induced and UV-induced damage-seq paper [1, 33] (Oligo sequences are in Supplementary Table S3). Briefly, cell pellet is resuspended in 200 μl of DPBS (Dulbecco's Phosphate Buffered Saline, Gibco, 14190-144)with 10 μl of RNase A (Thermo #EN0531), 20 μl of Proteinase K, and 200 μl of Buffer AL (both are from QIAGEN #69504). The suspension was then incubated at 55°C for 20 min, followed by purification with the QIAGEN DNeasy Blood & Tissue Kit (QIAGEN #69504) according to manufacturer's instruction. The purified genomic DNA is subsequently sonicated into 200–700 bp fragments with Covaris sonicator. The fragmented genomic DNA (∼2 μg) was used for end repair, 5′ phosphorylation, and dA-Tailing using 3 μl of End Prep Enzyme Mix and 7 μl of End Prep Reaction Buffer (NEB #E7546 or as included in NEB #E7645), at 20°C for 30 min and then 65°C for 30 min, before cooling down to room temperature. Following this, annealed AD1 adapter (500 pmol) was ligated to End Prepped DNA with 30 μl of Ligation Master Mix and 1 μl of Ligation Enhancer (NEB #E7595 or as included in NEB #E7645) at 16°C overnight. AD1 ligated DNA was purified with 1.2× AMPure XP beads and eluted in 50 μl of nuclease-free water. Before the incubation with antibody coated beads, AD1 ligated DNA was denatured into ssDNA with 20 μl of 8 M urea at 95°C for 1 min, then placed on ice for 1 min, and immediately incubated with antibody coated beads.

To prepare the antibody coated beads, 40 μl anti-rat Dynabeads (Thermo, #11035) was washed three times with 1 ml of 1× PEXB buffer (1× PBS, 2 mM EDTA, 0.01% Triton X-100, and 0.025% albumin). The beads were then incubated with 10 μg salmon sperm DNA (Thermo, #AM9680) and 1.5 μl of anti-cisplatin modified DNA antibody (Abcam, #ab103261) in 100 μl of 1× PEXB buffer at 4°C with rotation for 3 h. After incubation, antibody coated beads were then washed three times by 1 ml of 1× PEXB buffer and incubated with denatured, AD1 ligated DNA, and 10 μg salmon sperm DNA overnight at 4°C, to capture the oxaliplatin damaged DNA.

The beads were then washed subsequently with 400 μl of Wash Buffer U (20 mM Tris–HCl, pH 8, 2 mM EDTA, 1% Triton X-100, and 2 M urea), 400 μl of Wash Buffer II (20 mM Tris–HCl pH 8, 2 mM EDTA, 1% Triton X-100, 0.5 M NaCl, and 0.1% SDS), 400 μl Wash Buffer III (10 mM Tris–HCl pH 8, 1 mM EDTA, 150 mM LiCl, 1% IGEPAL CA-630, and 1% Na deoxycholate), 400 μl of Wash Buffer IV (100 mM Tris–HCl pH 8, 1 mM EDTA, 500 mM LiCl, 1% IGEPAL CA-630, and 1% Na deoxycholate), and 400 μl of 1× TE (10 mM Tris–HCl and 1 mM EDTA). The oxaliplatin damaged DNA fragments were then eluted from beads with 100 μl of Elution buffer [50 mM $NaHCO_3$, freshly prepared, 1% (w/w) SDS (Sodium dodecyl sulfate, Sigma, L3771)] at 65°C for 10 min. The eluted DNA was then precipitated by adding 10 μl of 3M sodium acetate solution, 1 μl of glycogen (Thermo #R0561), and 300 μl of ethanol at –80°C overnight.

Damage-seq library preparation

Ethanol precipitated DNA is dissolved in 7 μl of nuclease-free water. To this solution, Bio3U primer (30 pmol), 10 μl of Q5 Master Mix (NEB #M0544 or included in NEB #E7645) and nuclease-free water were added to reach a total volume of 20 μl. Primer extension is performed at 98°C for 45 s, followed by 65°C for 5 min, and then placed on ice for cooling. Next, 2 μl of Exo I (NEB, M0293S) was added to remove the excessive primers at 37°C for 10 min. The primer extended DNA is then purified with 2× AMPure XP beads, and eluted

with 30 μl of water. The DNA elute was denatured at 95°C for 90 s, and then immediately placed on ice for 2 min. The denatured DNA is subsequently incubated with 5 μl Streptavidin C1 beads (Thermo, #65001) in 30 μl of 2× B&W buffer [B&W final concentration (1×): 5 mM Tris–HCl pH 7.5, 1 mM EDTA, 1 M NaCl] at 4°C for 1 h to allow the biotinylated DNA being captured by C1 bead. The bead is then washed first with 100 μl of 1× B&W buffer, and then with 100 μl of 1× TE buffer. Finally the DNA was released from C1 beads into 18 μl of 0.1× TE by adding 2 μl of USER enzyme (NEB, #M5505) and incubating at 37°C for 25 min. The beads were washed by 25 μl of 1× B&W, and the supernatant was combined with the 20 μl of DNA elute obtained from the previous step.

To eliminate Bio3U extended DNA strand that read through the intact DNA fragment without damage (subtractive hybridization), Oligo SH (20 pmol) was added, followed by denaturing at 95°C for 1 min and naturally cooling down to room temperature to allow hybridization. Oligo SH hybridized product was then captured by adding 10 μl of Streptavidin C1 beads (resuspended in 60 μl of 1× B&W) for 1 h at 4°C. DNA was purified by ethanol precipitation at –80°C overnight.

To added second adapter to the 3′end, purified DNA was incubated with annealed AD2 (40 pmol) in 10 μl of 1× hybridization buffer (10 mM Tris–HCl, pH 7.5, 100 mM NaCl, and 0.1 mM EDTA) at 65°C for 10 min, and then 16°C for 5 min. After adding 10 μl of ligation mix (from Thermo #EL0013, 2 μl of 10× ligation buffer, 1 μl of T4 DNA ligase (HC), 1 μl of 50% PEG solution, and 1 μl of nuclease-free water), the AD2 ligation reaction is incubated at 16°C overnight. The ligation product was then purified by 2× AMPure XP beads and PCR (Polymerase chain reaction) amplified by Q5 Master Mix (NEB #M0544 or included in NEB #E7645S) for 13–16 cycles. The PCR products were purified with AMPure XP beads.

Hi-C library preparation and data processing

HCT116 OxR control cells Hi-C library was generated with the Arima-HiC kit (Arima Genomics, #A510008, Document #A160134 v01) and Arima Library Prep Module (Arima Genomics, Cat #A303011, Document #A160432 v02) following manufacturer's instruction. Raw sequencing data are processed following 4DN in-situ Hi-C data processing pipeline (https://data.4dnucleome.org/resources/data-analysis/hi_c-processing-pipeline).

Generation of population of genome structures from ensemble Hi-C data

The populations of diploid whole genome structures for the GM12878, HCT116 chemosensitive (HCT116 OxS), and HCT116 chemoresistant (HCT116 OxR) cell lines were generated from Hi-C data using our population-based genome structure modeling approach. GM12878 structures were taken from our previous publication [23]. HCT116 OxS cell Hi-C data were taken from Rao *et al.* 2017 [34]. Our approach is based on a data-deconvolution strategy and simulates a population of single-cell genome structures that statistically recapitulate the chromatin contact probabilities from experimental Hi-C data. To describe chromatin contacts in single cells and discriminate between homologous chromosome copies, we introduced latent variables that contain all missing information. Genome structure models are then generated by jointly optimizing both the latent variables and the coordinates of the structures, so that the input Hi-C data are statistically recapitulated by the models. This is a high-dimensional optimization problem, for which we adapted a hard Expectation-Maximization algorithm that uses a series of optimization strategies for efficient and scalable model estimation. More technical details can be found in [21, 22, 35]. Upon convergence, the resulting population consists of a population of single-cell 3D genome structures for GM12878 cells.

These models not only recapitulate ensemble Hi-C data with excellent agreement but also predict a variety of independent experimental data with high accuracy, both ensemble averaged data as well as cell-to-cell variability of single-cell structural features. Our model predict with high correlation [22, 23] average radial positions from GPSeq experiments [24], mean distances of chromatin regions to nuclear speckles from SON TSA-seq [25], contact frequencies between chromatin regions and the nuclear lamina from lamin B1 DamID [26], mean distances between chromatin regions and the lamin compartment at the nuclear envelope from lamin B1 TSA-seq experiments [25], speckle association frequencies (SAFs), and lamina association frequencies of genomic regions from DNA MERFISH multiplex imaging [27]. Simulated single-cell chromosome structures were also validated against single-cell structures from DNA MERFISH chromosome tracing experiments with excellent agreement [22, 23]. Thus, our genome structure models provide a valuable source of information about the structural microenvironment of genes in the nucleus.

Structural representation

The nucleus in our whole genome structure models is represented by a sphere with a radius $R = 5\mu m$ for GM12878 cells, and ellipsoid semi axes $a = 12350nm,\ \ b = 9640nm,\ \ c = 6920nm$ for HCT116 cells. Chromosomes are represented by a polymer chain model at 200 000 base-pair resolution. The full diploid genome is represented with a total of 30 332 genomic regions for GM12878 cell [23], and 30 906 genomic regions for HCT116 cells

Calculation of structure features from 3D genome structures

GM12878 structural features were taken from our previous publication [23], HCT116 structural features were calculated as described below (same as the method to calculate GM12878 structural features). Here, we summarize the key principles.

Mean radial position (RAD) of a chromatin region i is calculated as:

$$RAD_i = \frac{\sum_m^M \frac{r_{i,\,m}}{R}}{M}$$

Where M is the number of structures in population, $r_{i,\,m}$ is the distance of locus i to the nuclear center in structure m, and R represents the nucleus radius.

Interior localization frequency (ILF) of a chromatin region i is calculated as:

$$ILF_i = \frac{n_{r/R<0.5}}{M}$$

Where M is the number of structures in population, $n_{r/R<0.5}$ is the number of structures where either copy of the chromatin region i has a (normalized) radial position $\frac{r_i}{R} \leq 0.5$.

Locations of nuclear speckles or nucleolus in genome structures

In each genome structure chromatin regions known to interact most frequently with nuclear speckles (e.g. chromatin in the interior nucleus, $RAD < 0.5$)) where represented as a chromatin interaction network (CIN), where each node is a genomic region and an edge between two nodes is drawn if the corresponding regions physically interact in a given structure. Markov clustering (MCL-edge in the mcl tool [36]) is then performed to identify in this interaction network highly connected subgraphs with at leads 20 nodes. We showed that the geometric centers of all nodes in these selected highly connected subgraphs are a good representation of nuclear speckle locations in each single-cell genome structure. These models with predicted speckle locations can predict with good accuracy SON-TSA-seq experimental data, that measure the cytological distances between genomic regions and nuclear speckles at a genome-wide scale as well as SAFs from DNA MERFISH experiments [23]. Nucleolus locations were identified using nucleolus organizing chromatin regions [37] as input chromatin regions and same method for Markov clustering.

Average distance to the closest speckle (SpD)or nucleolus (NuD) refers to the average distance of a chromatin region i to the nearest predicted speckle (or nucleolus) location:

$$SpD_i = \frac{\sum_m^M SpD_{i,\,m}}{M},\ NuD_i = \frac{\sum_m^M NuD_{i,\,m}}{M}$$

Where M is the number of structures in the population, $SpD_{i,\,m}$ ($NuD_{i,\,m}$) is the distance of region i to the nearest speckle (or nucleolus) location in structure m.

SAF, lamina association frequency (LAF), and nucleolus association frequency of a chromatin region i are calculated as:

$$SAF_i\ (or\ NAF_i,\ LAF_i) = \frac{n_{d_i<d_t} + n_{d_i'<d_t}}{2M}$$

Where M is the number of structures in the population, $n_{d_i<d_t}$ is the number of structures, in which the first homologous copy of chromatin region i' has a distance to the nuclear body of interest (speckle, nucleolus, or lamina/nuclear periphery) smaller than the threshold distance (500 nm for speckle, $0.35R$ for lamina, and 1000 nm for nucleolus); $n_{d_i'<d_t}$ is the corresponding number of structures, in which the second homologous copy i' has a distance to the nuclear body of interest smaller than the threshold distance.

Predicted SON TSA-seq data and Lamin B1 TSA-seq data were calculated as described and taken from [23].

Local chromatin fiber decompaction (RG)

The local compaction of the chromatin fiber is estimated by the radius of gyration (RG) for a 1 Mb region centered at the locus:

$$RG_{i,\,m} = \sum_{j=1}^{N} d_{j,\,m}^2$$

Where N is the number of chromatin regions (depends on the resolution, for 200 kb region $N = 5$) in the 1-Mb window, and $d_{j,\,m}$ is the distance between the chromatin region j to the center of mass of the 1-Mb region, in the structure m.

Median *transA/B* ratio

We define the trans neighborhood $\{j\}$ of a chromatin region i as the set of regions from other chromosomes whose center-to-center distances to region i are <500 nm, which can be expressed as a set; $Ne_i^t = \{j : chrom_i \neq chrom_j,\ d_{ij} < 500nm\}$. The *transA/B* ratio can be expressed as:

$$TransA/Bratio_i = \frac{n_A^t}{n_A^t + n_B^t}$$

Where n_A^t and n_B^t are the number of *transA* and *B* regions in the set Ne_i^t for the region i. The median of the *transA/B* ratios for a given region is then calculated as the median value of all the *transA/B* ratios observed in the homologous copies of the region across all the structures.

Damage-seq data processing

We compare data from two types of DNA damage-seq experiments [4]. First, data from cultured cells (GM12878 or HCT116) treated with Pt drug, termed *in vivo* damage-seq data set. Second, control data of isolated DNA from cells treated with Pt drugs following the same procedure; we refer to this data set as the *in vitro* damage-seq data set.

Oxaliplatin damage-seq data were generated as previously described. Cisplatin damage-seq data were downloaded from https://www.ncbi.nlm.nih.gov/geo/query/acc.cgi?acc=GSE82213. Paired-ended fastq files of both data was trimmed by trimmomatic (v0.39) [38]. They were mapped to the human genome GRCh38 with HISAT2 (v2.2.0) [39] using parameter –rna-strandness RF –pen-noncansplice 1000000. Samtools (v1.0) [40] was used to convert the sam to bam files. After fixing mate pair with -mc parameter using samtools *fixmate* and sorting coordinates using samtools *sort*, reads were deduplicated by samtools *markup*. After PCR deduplication, only reads whose 5′ start are GG (for plus strand) or CC (for minus strand) are saved as potential cisplatin modified sites. R codes to extract the reads starting with GG and CC are described in Yimit *et al.* [41] and can be downloaded from https://github.com/yuchaojiang/damage_repair.

Binning

Data sets were binned to genomic windows of 200 kb, by counting the damage sites within each bin. To avoid bias due different sequencing depths, the number of damage sites per bin $N_i^{in-vivo}$ and $N_i^{in-vitro}$ (in bin i) are normalized by the median of ratio method as in DESeq2 paper [42].

In vivo damage enrichment value η

Differences between the DNA damage distribution of *in vivo* and *in vitro* samples reflect the effect of chromatin structure and its nuclear microenvironment on DNA damage susceptibility.

For a given 200 kb bin i, the *in vivo* damage enrichment value η_i is calculated as:

$$\eta_i = Log_2\left(\frac{N_i^{in\ vivo}}{N_i^{in\ vitro}}\right)$$

Where $N_i^{in\ vivo}$ and $N_i^{in\ vitro}$ are the normalized number of damage sites per bin i for the *in vivo* and *in vitro* settings, as defined above. η is the normalized damage level for bin and used for the visualization of DNA damage in 3D genome structure (Fig. 3C).

Detection of significantly enriched *in vivo* damage sites (EN) and significantly depleted (DP) damage sites

Significantly enriched *in vivo* DNA damage sites (EN) are defined as bins with $\eta_i > 1$ and FDR < 0.05, while significantly depleted *in vivo* DNA damage sites (DP) are defined as bins with $\eta_i < 1$ and FDR < 0.05. All other bins are referred to as *unchanged regions*.

ChromHMM state analysis

ChromHMM annotates chromatin in GM12878 cells based on epigenetic features into 15 ChromHMM states {i.e. Active promoter, Strong enhancer …}. We partitioned the genome into a series of sequence intervals, each composed by consecutive bases with the same ChromHMM state annotation [43]. The mean radial position (RAD) of an interval is calculated from the corresponding genomic regions in the genome structure models. All ChromHMM intervals were stratified into five groups {0, 1, 2, 3, 4} according to their mean radial positions. For example, intervals in quintile group 0 are those with the lowest 20% RAD values.

The *in vivo* damage enrichment value η for a particular interval i with ChromHMM state h and RAD quintile group r is calculated as:

$$\eta_{i,\,h,\,r} = Log_2\left(\frac{N^{in\ vivo}_{i,\,h,\,r}}{N^{in\ vitro}_{i,\,h,\,r}}\right)$$

Where $N^{in-vivo}_{i,\,h,\,r}$ is the normalized number of *in vivo* damage sites in interval i that belong to ChromHMM state h and RAD group r, i={0, 1, 2…n} are all intervals that belong to the particular ChromHMM state h={1, 2, …H}.; $N^{in-vitro}_{i,\,h,\,r}$ is the corresponding normalized number of *in vitro* damage sites. Normalization is performed by DESeq2 [42].

To generate the barplot in Fig. 4, the median *in vivo* damage enrichment value $M_{h,\,r}$ for a given ChromHMM state h and radial group r is calculated as follows:

$$M_{h,\,r} = Median(\{\eta_{1,\,h,\,r},\ \eta_{2,\,h,\,r}\cdots\eta_{n,\,h,\,r} | For\ all\ \eta_{i,\,h,\,r} \in ChromHMM\ state\ h\ and\ RAD\ group\ r\})$$

Calculating enrichment of DP and EN regions in Hi-C compartments

The enrichment fold of EN regions in a compartment s is calculated as follows:

$$F^{compartment}_{s}(EN) = \frac{N^{compartment}_{s}(EN)}{\left\langle C^{compartment}_{s}(EN)\right\rangle}$$

- Where $N^{compartment}_{s}(EN)$ represents the number of EN regions in compartment s, where s is either the A or B compartment.
- $< C^{compartment}_{s}(EN) >$ is the expected number of EN regions in compartment s, estimated as the average number of EN regions in compartment s from 10 000 random permutations of EN regions across the genome.
- For each permutation, we determine $C^{compartment}_{s}(EN)$ as the number of EN regions in compartment s, creating a null distribution of expected counts. The observed $N^{compartment}_{s}(EN)$ is then compared against this distribution. The P-value enrichment fold $F^{compartment}_{s}(EN)$is calculated as the proportion of permutations where $C^{compartment}_{s}(EN)$ is greater than or equal to $N^{compartment}_{s}(EN)$.

$$p - value = (Number\ of\ permutations\ with\ C^{compartment}_{s}(EN)\ \geq N^{compartment}_{s}(EN))/10000.$$

The enrichment of DP regions in a compartment s is calculated accordingly as:

$$F^{compartment}_{s}(DP) = \frac{N^{compartment}_{s}(DP)}{< C^{compartment}_{s}(DP) >}$$

Calculating enrichment of DP and EN regions in Hi-C subcompartments

The enrichment fold of EN rand DP regions in a subcompartment s is calculated accordingly as:

$$F^{subcompartment}_{s}(EN) = \frac{N^{subcompartment}_{s}(EN)}{\left\langle C^{subcompartment}_{s}(EN)\right\rangle}$$

$$F^{subcompartment}_{s}(DP) = \frac{N^{subcompartment}_{s}(DP)}{< C^{csubompartment}_{s}(DP) >}$$

where s is either the A1, A2, B1, B2, or B3 subcompartment as defined in Rao *et al.* [44].

Calculating the enrichment of DP and EN regions for each Hi-C compartment stratified over RAD or SpD quintile groups

DP and EN regions are categorized into two groups $s \in$ {A, B} according to their compartment annotation. Then each compartment group was classified into five RAD quintiles groups r = {0, 1, 2, 3, 4} according to their mean radial positions (RAD) in the genome structure population. The enrichment fold of EN regions at a particular RAD quintile group r and compartment s is calculated as:

$$F^{RAD}_{s,\,r}(EN) = \frac{N^{RAD}_{s,\,r}(EN)}{< C^{RAD}_{s,\,r}(EN) >}$$

Where $N^{RAD}_{s,\,r}(EN)$ is the number EN regions that belong to the RAD quintile group $r\in$ {0, 1, 2, 3, 4} and compartment $s \in$ {A, B}. $< C^{RAD}_{s,\,r}(EN) >$ is the random control calculated as the average number of EN regions within RAD quintile group r and compartment s across 10 000 randomly selected permutations of EN regions across the genome.

The enrichment fold of DP sites at a RAD quintile group r and compartment s is calculated accordingly as:

$$F^{RAD}_{s,\,r}(DP) = \frac{N^{RAD}_{s,\,r}(DP)}{< C^{RAD}_{s,\,r}(DP) >}$$

where, $N^{RAD}_{s,\,r}(DP)$ is the number DP sites that belong to a particular RAD quintile group r and compartment s. $< C^{RAD}_{s,\,r}(DP) >$ is the random control calculated as the average number of DP sites within RAD quintile group r and compartment s across 10 000 randomly selected permutations of DP sites across the genome.

To calculate the fold enrichment of EN regions at various speckle distances (SpD), DP and EN regions are first categorized into two compartment groups $s\in$ {A, B} according to their compartment annotation. For each compartment group EN regions were classified into quintiles $p \in$ {0, 1, 2, 3, 4} based on their average speckle distances (SpD) in the genome

structure population. The fold enrichment of EN regions at a particular SpD quintile group p and compartment s is calculated as:

$$F^{SpD}_{s,\,p}\,(EN) = \frac{N^{SpD}_{s,\,p}\,(EN)}{< C^{SpD}_{s,\,p}\,(EN) >}$$

With $N^{SpD}_{s,\,p}$ as the number of EN regions that belong to a SpD quintile group p and compartment s. $< C^{SpD}_{s,\,p}(EN) >$ is the random control calculated as the average number of EN regions within SpD quintile group p and compartment s across 10 000 randomly selected permutations of EN regions across the genome.

The fold enrichment of DP regions at a SpD quintile group p and for compartment s is calculated accordingly as:

$$F^{SpD}_{s,\,p}\,(DP) = \frac{N^{SpD}_{s,\,p}\,(DP)}{< C^{SpD}_{s,\,p}\,(DP) >}$$

where, $N^{SpD}_{s,\,p}$ is the number of DP regions that belong to SpD quintile group p and compartment s. $< C^{SpD}_{s,\,p}(DP) >$ is the random control calculated as the average number of DP sites within SpD quintile group p and compartment s across 10 000 randomly selected permutations of DP sites across the genome.

Calculate the enrichment of feature values from experimental dataset and 3D genome structures for genomic regions at DP, EN, and unchanged regions

We calculated the fold enrichment of several features derived from either 3D genome structures, histone modifications, or TSA-seq experiments. Histone modification and TSA-seq data sets where binned to make them comparable to 3D genome structure features. Binning was performed with the pyBigWig python package by computing the mean signal over each 200 kb genomic window.

Feature values are normalized to a range of 0 and 1 using min–max normalization. The normalized signal is then used to calculate the enrichment fold $F^{feature}_e$ of feature $e = \{RAD,\ SpD,\ histone\ ChIP-seq,\ TSA-seq\cdots\}$.

The enrichment fold of a specific feature value in EN regions is calculated as:

$$F^{feature}_e\,(EN) = \frac{N^{feature}_e\,(EN)}{< C^{feature}_e\,(EN) >}$$

Where $N^{feature}_e(EN)$ is the mean feature value in EN regions. $< C^{feature}_e(EN) >$ is the random control as the mean feature value calculated from randomly permuted EN regions across the genome. The permutation is conducted 100 times.

The following feature values were analyzed: (i) genome structure features: RAD, ILF, SpD, NuD, NAF, LAF, RG, and ICP transAB, (ii) TSA-seq data (LaminaA/C TSA-seq, Lamin B1 TSA-seq, pSC35 TSA-seq, and ON TSAA-seq; (iii) histone modifications (H3K36me3, H3K27me3, H3K9me2, H3K9me3, H3K9ac, H4K20me1, H3K4me1, H3K4me2, H3K4me3, H3K27ac, H2AFZ, and H3K79me2). For distance metrics like RAD, SpD, and NAD, we use 1- RAD, 1 -SpD, and 1-NAD to calculate $F^{feature}_e$.

Similarly, the enrichment fold for a specific feature in DP regions is calculated as:

$$F^{feature}_e\,(DP) = \frac{N^{feature}_e\,(DP)}{\left\langle C^{feature}_e\,(DP)\right\rangle}$$

Where $N^{feature}_e(DP)$ is the mean feature value in DP sites and $< C^{feature}_e(DP) >$ as the random control as described above.

Correlation between experimental XR-seq data and *in vivo* damage enrichment values as well as 3D genome structure features

XR-seq data is binned at 200 kb. The scipy.stat module is used to compute the Spearman correlation, the p-value, and R value between *in vivo* damage enrichment values η and XR-seq signal and between 3D genome features and η. Stat.linregress function is used to compute the slope, and intercept in linear regression. Stat.gaussian_kde is used to estimate the the density of scattered dots in scatter plots.

Calculation of partial correlation between *in vivo* damage enrichment values, radial positions and ATAC-seq signals

We used the partial correlation method [45] to computes the correlation between two variables x and y conditioning on the third variable z. This partial $r_{xy,\,z}$ can be formulated as:

$$r_{xy,\,z} = \frac{r_{xy} - r_{xz}r_{yz}}{\sqrt{\left(1-r^2_{xz}\right)\left(1-r^2_{yz}\right)}}$$

Where r_{ij} represents the correlation between any two variables $i,\ j \in \{x,\ y,\ z\}$, which can be either Pearson's or Spearman's. Here x represents *in vivo* damage enrichment value, y represents chromatin accessibility, z represents radial position for every 200 kb genomic bin. Using partial_corr function in the Pingouin python package, we calculated the partial correlation between *in vivo* damage enrichment values and chromatin accessibility conditioning on radial position ($r_{xy,\,z}$), and the partial correlation between *in vivo* damage enrichment values and radial positions conditioning on chromatin accessibility ($r_{xz,\,y}$), Spearman correlation is used here for computing partial correlation and p-value.

Gene Ontology and expression analysis

Genes whose TSS in EN or DP regions were extracted for Gene Ontology analysis using Gene Ontology webserver (http://geneontology.org), for the GO terms with enrichment fold > 1, top 11 terms with lowest FDR were selected as representative terms

Results

We study the role of the nuclear microenvironment on the susceptibility of DNA for Pt drug-induced damage. To achieve this goal, we combine Pt drug-induced DNA-damage data from DNA damage-seq experiments (Fig. 1A) with information about the locations of chromosomal regions within the nuclear topography from a population of single-cell 3D genome structures, generated from Hi-C data using the Integrative Genome Modeling (IGM) platform [22, 23] (Fig. 1B)

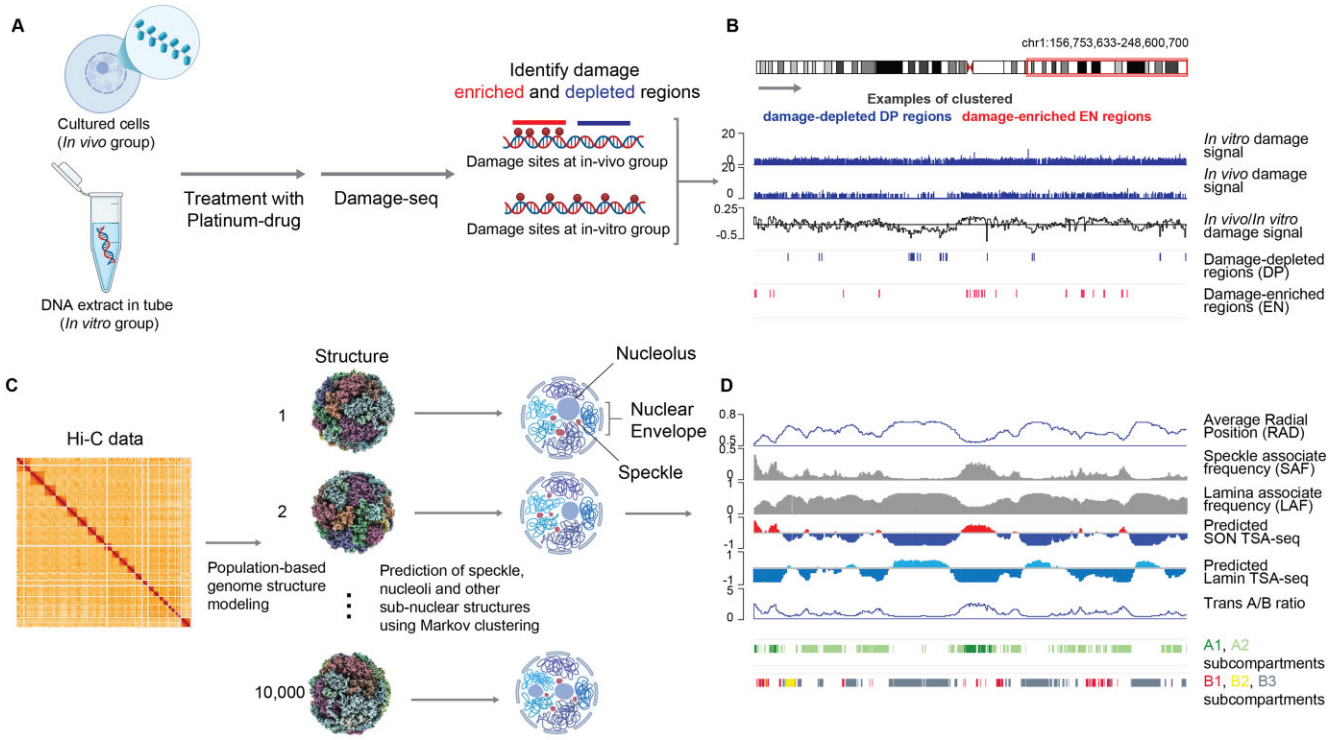

Figure 1. Illustration of the workflow. (**A**) Schematic view of damage-seq experiments in GM12878 cells. *In vivo* damage-seq was performed on intact nuclei, while *in vitro* data were generated from isolated DNA extracts. Damage enriched and depleted regions were identified by comparing the damage signal between the *in* vivo and *in vitro* groups. (**B**) Results of damage-seq experiments (first profile from the top). *In vitro* damage-seq signal is relatively uniformly distributed at genome (second profile from the top). *In vivo* damage-seq signal is not uniformly distributed, reflecting the impact of chromatin structure and the nuclear microenvironment (third profile from top). To quantitively measure how chromatin structure and nuclear microenvironment modulate DNA damage susceptibility. *In vivo* damage enrichment value for a given 200 kb bin is calculated as the ratio of *in vivo*/*in vitro* damage signal in this bin (fourth profile from the top). Damage-depleted regions (DP) are chromatin regions with significantly reduced DNA damage signals in *in vitro* in comparison to *in vivo* damage-seq experiments (fifth profile from the top). Damage-enriched regions (EN) are chromatin regions with significantly increased DNA damage signals in *in vitro* in comparison to *in vivo* damage-seq experiments. (**C**) Generation of 3D genome structures from Hi-C data by population-based genome structure modeling as described in [22, 23]. Extraction of spatial features from the population of 10 000 genome structures (see Materials and methods and [23] for details). Structures are used to predict location of nuclear bodies and a variety of structural features that characterize the nuclear microenvironment of each genomic region in the genome. We combine this information with cisplatin-damage-seq data to assess the impact of the nuclear environment on the DNA damage susceptibility of genomic regions. (**D**) Structural features calculated from 3D genome structures: (first profile from the top) mean radial position (RAD), (second profile from the top) SAF, (third profile from the top) LAF, (fourth profile from the top) predicted SON-TSA seq, (fifth profile from the top) predicted Lamina-TSA seq, and (sixth profile from the top) median *transA*/*B* ratio (seventh and eighth profile from the top) Hi-C subcompartments annotation, providing spatial information and functional connection of chromatin within the cell nucleus. Overall, combining the structure features with damage-seq result (Fig. 1B) illustrate the influence of chromatin structure and nuclear microenvironment on cisplatin-induced DNA damage susceptibility.

(Materials and methods). Our study focuses on lymphoblastoid cells (GM12878), for which cisplatin damage-seq experiments are available for both *in vivo* (DNA-damage seq in intact nuclei) and *in vitro* experiments (DNA-seq from isolated DNA extracts) [4]. Then, we study the 3D nuclear distribution of oxaliplatin drug-induced DNA damage in drug sensitive HCT116 OxS and drug resistant HCT116 OxR cancer cell lines to investigate if chemoresistance coincides with a redistribution of DNA damage in the 3D genome structures.

The nuclear microenvironment affects cisplatin induced DNA damage susceptibility of genomic regions

We first identified chromatin regions that showed significantly altered DNA damage between *in vitro* and *in vivo* damage-seq experiments in GM12878 cells. *In vivo* damage-seq experiments were performed on intact nuclei, while *in vitro* damage-seq data were generated from isolated DNA extracts [4] (Fig. 1A). GM12878 cells were treated with cisplatin at a concentration of 200 μM for 1.5 h [46]. This dosage is ∼10-fold higher than the IC_{50} for cisplatin in cells [47] to ensure that robust damage signal was detected. Differences in damage-seq signals between both groups reflect the effect of chromatin structure and nuclear microenvironment on cisplatin-induced DNA damage (Fig. 1B). Visual inspection confirms that *in vitro* DNA damage is more uniformly distributed across the genome compared to *in vivo* DNA damage in intact nuclei (Fig. 1B). To identify regions with significantly altered damage-seq signals between *in vitro* and *in vivo* experiments, we divided the genome into consecutive 200 kb bins [4]. Among the resulting 15 161 bins with DNA damage sites a total of 2292 (15.1%), showed significantly different cisplatin-induced damage between *in vivo* and *in vitro* conditions (FDR < 0.05, using the statistical module in DESeq2 from two biological replicates [42] (Supplementary Table S1) (Materials and methods) (Fig. 2A). Specifically, 1006 regions (6.6%) showed significantly lower damage in the *in vivo* damage-seq data compared to isolated *in vitro* DNA extracts (Supplementary Table S1). These regions are more protected

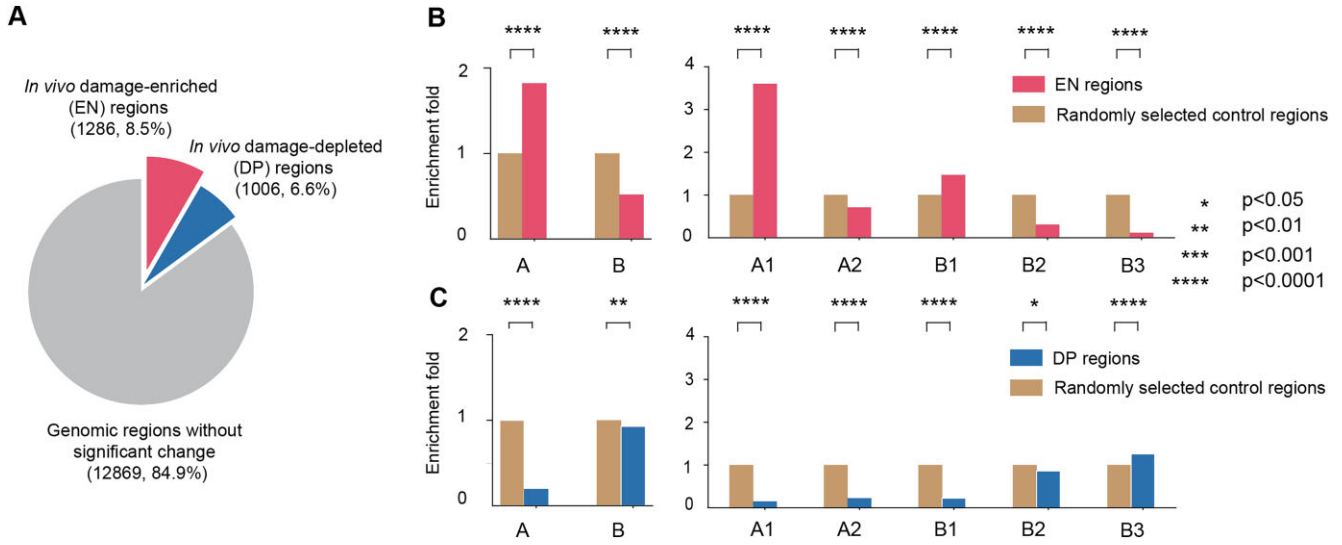

Figure 2. Enrichment of EN/DP chromatin regions in different (sub)compartments, (**A**) Number and percentage of *in vivo* damage-enriched (EN) and -depleted regions (DP). (**B**) Left panel, in each pair of bars, the right-hand bar represents enrichment fold of EN regions (i.e. *in vivo* damage-enriched regions) for chromatin in different compartments and the left-hand bar indicates the corresponding control regions. Right panel, in each pair of bars, the right-hand bar represents enrichment fold of EN regions for chromatin in different subcompartments and the left-hand bar indicates the corresponding control regions [44]. (* $p<0.05$, ** $p<0.01$, *** $p<0.001$, **** $p<0.0001$) Brown bars represent enrichment folds of random selected control regions for chromatin in different compartments or subcompartments, respectively. (**C**) Left panel, in each pair of bars, the right-hand bar represents enrichment fold of DP regions (i.e. *in vivo* damage-depleted regions) for chromatin in different compartments and the left-hand bar indicates the corresponding control regions. Right panel, in each pair of bars, the right-hand bar represents enrichment fold of DP regions for chromatin in different subcompartments and the left-hand bar indicates the corresponding control regions.

from DNA damage in the nuclear context (Fig. 2A). We name these regions "*in vivo* damage-depleted" (DP) regions. Conversely, 1286 genomic regions (8.5%) were significantly enriched for DNA damage *in vivo* compared to *in vitro* damage-seq data (Supplementary Table S1), indicating greater susceptibility to DNA damage within the nucleus in comparison to isolated DNA. We refer to these regions as "*in vivo* damage-enriched" (EN) regions (Fig. 2A).

Differential cisplatin-damaged regions are enriched in specific chromatin compartments

One of our goals is to understand how the nuclear microenvironment influences DNA damage susceptibility, either enhancing or decreasing it for specific regions compared to isolated DNA. To investigate this, we examined if EN and DP regions are preferentially associated with distinct functional chromatin compartments (Figs 1B and 2B). Genome-wide Hi-C data classify chromosomal regions into two functional compartments: the transcriptionally active A and the inactive B compartment. Regions within the same compartment exhibit higher contact frequencies, while interactions between compartments are less frequent [48]. Our analysis revealed that EN regions are enriched in the more open, active A compartment and depleted in the B compartment (Fig. 2B, left panel). In contrast, DP regions are depleted in the A compartment and only slightly depleted in the B compartment (Fig. 2C, left panel).

To further investigate these patterns, we assessed if EN and DP regions are statistically enriched or depleted in Hi-C subcompartments. Rao *et al.* [44] used machine learning to Hi-C data to classify chromatin into five dominant subcompartments: two associated with active chromatin (A1 and A2) and three inactive subcompartments (B1, B2, and B3). Each subcompartment shows distinct characteristics in terms of epigenetic features and replication timing. Active subcompartments (A1 and A2) are marked by activating chromatin modifications. A1 is gene-rich, contains the most highly expressed genes, and replicates early, while A2, replicates into mid-S phase and contains on average longer genes than A1. Subcompartments (B1, B2, and B3) correlate with inactive chromatin. B1 is marked by H3K27me3 (facultative heterochromatin) and B2 is enriched in pericentromeric heterochromatin, nucleolus-associated domains (NADs) and nuclear lamina, while B3 is enriched in lamina-associated domains (LADs) but depleted at NADs. Both B2 and B3 replicate late in S phase.

To evaluate transcriptional activity across subcompartments, we calculated the mean Transcripts Per Million (TPM) of genes within 200 kb bins of each subcompartment (Supplementary Fig. S1). In GM12878 cells, the A1 and A2 subcompartments show higher transcriptionally activity than the three B subcompartments, with genes in A1 being significantly more transcribed than those in A2 (Supplementary Fig. S1). While A2 is less active than A1, it remains significantly more transcriptionally active than all three B subcompartments. Notably, genes in the B1 subcompartment have significantly lower transcriptional activity than A2 (Supplementary Fig. S1).

Interestingly, EN regions are not only significantly enriched in the active A1 subcompartment but are also moderately enriched in the silenced B1 subcompartment. In contrast, they are slightly underrepresented in the transcriptionally more active A2 subcompartment, and strongly depleted at inactive B2 and B3 subcompartments (Figs 1B and 2B, right panel). These patterns indicate that transcriptional activity alone cannot fully explain variations in DNA susceptibility to cisplatin-induced damage. DP sites are generally underrepresented across all subcompartments, except for the B3 sub-

compartment, which corresponds to lamina-associated heterochromatin [44] (Fig. 2C, right panel).

Cisplatin damage of chromatin is correlated with their nuclear positions

Next, we analyzed the nuclear locations of EN and DP sites within the nuclear topography, namely their locations with respect to nuclear speckles, nucleoli and the lamina compartment at the nuclear envelope. Information about the nuclear organization is extracted from a population of 10 000 diploid single-cell 3D genome structures generated from Hi-C data by our population-based IGM genome structure modeling method (Fig. 1C) [23]. We demonstrated that our 3D genome structures predict with good accuracy the nuclear locations of genomic regions as assessed by a variety of independent experimental data, including the mean distances of genomic regions to nuclear speckles from SON-TSA-seq data, association frequencies to nuclear speckles from DNA MERFISH experiments, mean distances to the lamin compartment from lamin B1 TSA-seq data, contact frequencies to lamin compartment from pA-lamin B1 DamID data, and radial positions of genomic regions from GPSeq data [23]. Thus, we predicted five structural features for each genomic region, characterizing its nuclear microenvironment: radial position in the nucleus (RAD), distance to the nearest nuclear speckle (SpD), distance to the nearest nucleolus (NuD), local chromatin fiber decompaction (RG), and the median *transA/B* compartment ratio (*Trans A/B*). Additionally, we measured four population-level frequencies: ILF, SAF, nucleoli association frequency (NAF), and LAF (Fig. 1D, see Materials and Methods). Some structural features like RAD and ILF are interrelated, as they both describe aspects of a locus's spatial position within the nucleus. While these measures are correlated, they each capture distinct aspects of nuclear organization. Considering them together provides a more comprehensive understanding of nuclear architecture than either metric alone.

We first studied the role of nuclear positions on DNA damage susceptibility. The average radial position (RAD) of genomic regions (and their interior localization probability (ILF)) show high and significant correlations with *in vivo* damage enrichment values (Fig. 3A and B) (RAD: Spearman corr = −0.72, *P*-value∼0 and ILF: Spearman corr = 0.72, *P*-value∼0). Mapping the *in vivo* damage enrichment values onto a representative single-cell 3D genome structures (Fig. 3C, left panel) also depicts increased cisplatin damage levels toward the nuclear interior and depleted levels at the nuclear periphery (Fig. 3C, left panel). However, since EN regions are enriched in the A compartment, which has a higher probability to be located toward the nuclear interior, we analyzed the role of the radial positions separately for chromatin in the A and B compartment. We stratified chromatin in each compartment into five quintiles based on their average radial positions. For both compartments, EN regions are strongly enriched toward the nuclear interior (Fig. 3D, left panel), with the highest EN enrichment observed in the most interior radial shell (quintile 0) (Fig. 3D, left panel). Conversely, DP regions showed the opposite trend, with strong enrichment toward the nuclear periphery in both A and B chromatin (Fig. 3E, left panel).

Our findings also explain why both transcriptionally active A1 and silenced B1 subcompartment chromatin are enriched in EN regions, whereas the transcriptionally active A2 subcompartment lacks this enrichment. Both, A1 and B1 chromatin are both preferentially localized toward the nuclear interior, while A2 chromatin lacks this preference and shows greater cell-to-cell variability in nuclear locations (Supplementary Fig. S1 and Fig. 2B, right panel). B1 chromatin is enriched in repressive H3K27me3 histone modifications and transcriptionally silenced [44]. Compared to A1, EN enrichment at B1 is modest, which may be attributed to B1's slightly larger cell-to-cell variability of its nuclear positioning (Supplementary Fig. S2). Thus, independent of transcriptional status, the nuclear position of a genomic region appears to be an important factor for EN region enrichment, and thus DNA damage susceptibility.

To validate our findings, we analyzed data from GPSeq experiments, a genomic profiling technology that maps the average radial positions of genomic regions in haploid HAP1 cells [24]. Despite the difference in cell type, we found that the average radial positions of genomic regions are well conserved between HAP1 and GM12878 cells (Pearson's *r*: 0.80) [23]. We therefore stratified the 200 kb genomic regions into quintiles based on their GPSeq-defined radial position [24]. Using GPSeq data, we found almost identical enrichment profiles for EN and DP regions across all radial position quintiles (Supplementary Fig. S3A and B), confirming the results obtained from our genome structure models in GM12878 cells. Thus, DNA damage susceptibility is indeed strongly correlated with nuclear position, independent of the chromatin compartment.

It is unclear what physical mechanism underlies the preferred interior positions of damage enriched EN regions. It has been established that some nuclear bodies, such as nuclear speckles and polycomb bodies, show preferences in their locations toward the nuclear interior and are excluded from the nuclear periphery [28, 29]. This raises the possibility that enriched DNA damage in specific nuclear environments may result from the preferred colocalization of genomic regions with nuclear bodies that may contain an increased concentration of cisplatin. To explore this, we investigated if preferred colocalization with nuclear speckles could equally well, or even better explain the observed enrichment patterns of damage-seq signals in chromatin regions with interior radial positions.

Our modeling approach predicts with good accuracy the locations of nuclear speckles and nucleoli in each single-cell genome structure model [22, 23]. To determine locations of nuclear speckles in each single-cell genome structure, we determined highly connected clusters of speckle associated chromatin following our established approach [23]. The geometric centers of these clusters represent good approximations of nuclear speckle locations in single-cell models [23], as demonstrated by the prediction of experimental SON TSA-seq data from our models with high correlation (Pearson's $r = 0.87$ [23] [25] (SON TSA-seq data measure the mean distances between genomic regions and speckles) [25]. Our models also predicted SAFs of genomic regions with high correlation to SAF measured in multiplexed FISH imaging [27] (Pearson's $r = 0.77$ [23].

In vivo damage enrichment values showed a high correlation with the SAF and mean speckle distances (SpD) of genomic regions (Fig. 3F and G) (SAF: Spearman corr = −0.72, *P*-value∼0 and SpD: Spearman corr. = −0.69, *P*-value∼0). Peaks in the predicted SAF profile align well with the sequence locations of EN regions (Fig. 1, right panel). Moreover, in individual chromosome structures increased DNA damage signals

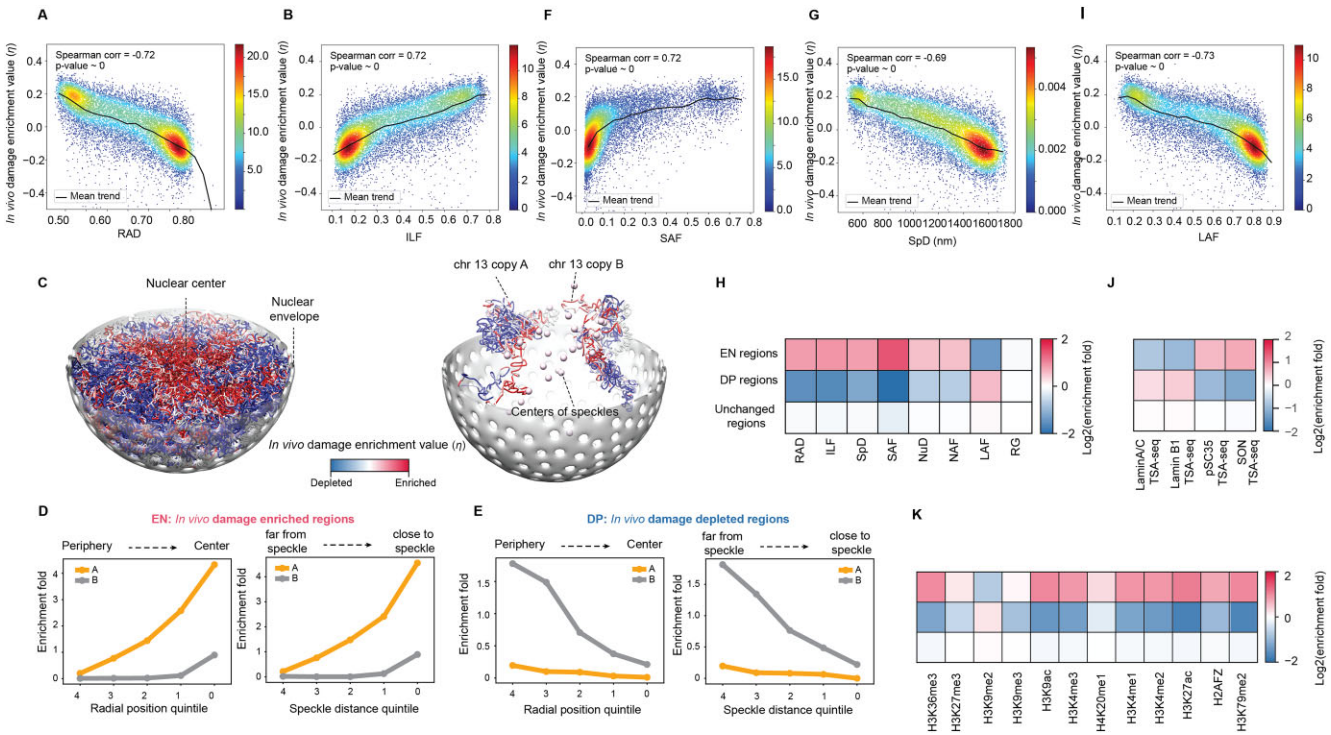

Figure 3. The role of a genomic region's nuclear position in cisplatin DNA damage susceptibility The distribution of cisplatin-induced DNA damage in the genome correlates with features of the nuclear organization, including nuclear positioning, subnuclear structures, and histone modification. (**A**) Scatter plot of the average radial position (RAD) of each genomic region derived from the 3D genome structure population and its *in vivo* damage enrichment value derived from damage-seq experiments. (**B**) Scatter plot of the ILF of each genomic region derived from the 3D genome structure population and its *in vivo* damage enrichment value derived from damage-seq experiments. (**C**) (Left panel) Visualization of the 3D genome distribution of cisplatin DNA damage enrichment. Cisplatin *in vivo* DNA damage enrichment value is mapped onto a representative whole diploid 3D genome structure at 200 kb resolution. (Right panel) Visualization of the 3D distribution of cisplatin DNA damage enrichment values in two copies of chromosome 13 together with the predicted locations of nuclear speckles (spheres) from the same 3D genome structure as in the left panel. (**D**) (Left panel) Enrichment folds of EN regions in A versus B compartments at different radial positions in 3D genome structures. EN regions are divided into quintiles based on their average radial position in the model population. (Right panel) Enrichment folds of EN regions observed in A versus B compartments at different distances to the closest nuclear speckle in 3D genome structures. EN regions are divided into quintiles based on their average speckle distance in the model cell population. (**E**) (Left panel) Enrichment folds of DP regions in A versus B compartments at different radial positions in 3D genome structures. DP regions are divided into quintiles based on their average radial position in the model population. (Right panel) Enrichment folds of DP regions in A versus B compartments observed at different distances to the closest nuclear speckle in 3D genome structures. DP regions are divided into quintiles based on their average speckle distance in the model cell population. (**F**) Scatter plot of the SAF of each genomic region derived from the 3D genome structure population and its *in vivo* damage enrichment value derived from damage-seq experiments. (**G**) Scatter plot of the average speckle distance (SpD) of each genomic region derived from the 3D genome structure population and its *in vivo* damage enrichment value derived from damage-seq experiments. (**H**) Enrichment fold heatmaps of several structural features calculated from the 3D genome structures at 200 kb base-pair resolution for EN (top row), DP (middle row) and regions without significant damage change (bottom row). (**I**) Scatter plot of the LAF of each genomic region derived from the 3D genome structure population and its *in vivo* damage enrichment value derived from damage-seq experiments. (**J**) Enrichment heatmaps for various TSA-seq data from TSA-seq experiments of K562 cells for EN (top row), DP (middle row), and regions without significant damage change (bottom row), 200 kb resolution. SON, pSC25 are speckle markers. TSA-seq provides information about the median distance of a genomic region to a nuclear compartment (speckles or lamins). (**K**) Enrichment heatmaps of histone modifications from ChIP-seq experiments for EN (top row), DP (middle row), and regions without significant damage change (bottom row), 200 kb resolution (Materials and methods).

are preferentially found toward nuclear speckle locations as shown in a representative genome structure models (Fig. 3C, right panel, using 2 homologues copies of chromosome 13 as example).

Regions with cisplatin-indued DNA damage are enriched in specific nuclear microenvironments

To better characterize the nuclear microenvironment of genomic regions, we calculated a set of additional structural features from 3D genome structures, delineating their spatial positioning within the nuclear topography in single-cell models. Besides the radial position (RAD) of a genomic region and its distance to the nearest nuclear speckle (SpD), we calculated the distance to the nearest nucleolus (NuD) and measured the frequency at which a genomic region associates to the lamina compartment at the nuclear envelope, a nuclear speckle or a nucleolus. These association frequencies—termed LAF, SAF, and NAF, respectively—represent the fraction of occurrences in proximity of these nuclear compartments [23]. We also determined the local chromatin fiber decondensation by calculating the radius of gyration for chromatin 500 kb upstream and downstream from a locus (RG), along with the fraction of A and B compartment chromatin for these inter-chromosomal encounters (*trans A/B* ratio) (Materials and methods).

We then calculated the fold enrichment of each structural feature and association frequency in EN and DP genomic regions (Fig. 3H). EN and DP regions show opposite enrichment patterns. EN regions are enriched in genomic regions with smaller RAD and SpD values and higher SAF, ILF, and

NAF values, with SAF showing the highest log fold enrichment (Fig. 3H). In contrast, DP regions are characterized by larger RAD and SpD values and overall lower SAF, ILF, and NAF values.

Among all features, *in vivo* damage enrichment correlates most strongly with SAF (Fig. 3F) (Spearman corr = 0.72, *P*-value∼0). This aligns with recent findings that cisplatin concentrations can be significantly enriched in nuclear speckles, other nuclear bodies and transcriptional condensates [14, 15]. Since nuclear speckles are preferentially located toward the nuclear interior, radial positions and speckle distances are naturally correlated. Thus, the increased cisplatin concentrations at nuclear speckles could therefore provide a rationale for the enhanced DNA damage susceptibility of EN regions in the nuclear interior and enhanced *in vivo* damage over isolated DNA.

In contrast, high lamina association frequencies (i.e. LAF values) are strongly enriched in DP and depleted in EN regions (Fig. 3H). Consistently, the LAF is strongly anticorrelated with *in vivo* damage enrichment values (LAF: Spearman corr = −0.73, *P*-value∼0) (Fig. 3I), confirming that regions located at the nuclear periphery are more protected from DNA damage than those in DNA extracts.

We validated our findings with data from Tyramide Signal Amplification sequencing (TSA-seq) [25] experiments (Fig. 3J). TSA-seq is a genomic mapping technique that estimates mean chromosomal distances from nuclear bodies and compartments, such as nuclear speckles (SON-TSA-seq) or the nuclear lamina (lamina-TSA-seq) [25]. For example, SON-TSA generates a gradient of diffusible tyramide free radicals at speckle locations, labeling nearby DNA. The amount of labeled DNA obtained from sequencing can then be translated into mean distances to speckles using an exponential diffusion model. Because TSA-seq data is not available for GM12878 cells, we used available TSA-seq data for the related K562 leukemia cell line [25]. Lamin A/C and B proteins are located at the nuclear periphery linking specific chromatin regions to the nuclear envelope. Lamin A/C and Lamin B TSA-seq experiments measure the mean distance of genomic regions from the nuclear lamin compartment. The enrichment of these data in DP regions confirm our predictions that DP sites are preferentially located at the nuclear periphery while EN regions are depleted in lamina exposed chromosomal regions (Fig. 3J). The proteins SON and pSC35 are marker proteins for nuclear speckles. SON TSA-seq and pSC35 TSA-seq experiments therefore measure the mean distances of genomic regions to nuclear speckles. We found that EN regions have elevated SON, and pSC35-TSA-seq values, supporting our predictions that EN regions show small average distances to nuclear speckles. In contrast, DP regions are depleted in speckle-related TSA-seq data, confirming our predictions that these regions show on average a relatively larger distance to nuclear speckles (Fig. 3J).

To validate that TSA-seq data from K562 cells are a good proxy for GM12878 cells, we also predicted SON and Lamin B1 TSA-seq data from our 3D genome structure models of GM12878 cells following a previously developed procedure [22, 23] (Fig. 1D). These predicted TSA-seq profiles are almost identical to those of K562 cells with high correlations (SON TSA-seq: Spearman corr = 0.89, LaminB1 TSA-seq: Spearman corr = 0.81) [23], confirming the overall similarity of TSA-seq data from K562 and GM12878 cells.

Finally, to further validate the link between speckle proximity and cisplatin-induced damage, we used HiCAN, a software tool that extracts speckle and nucleolus components from Hi-C contact matrices via non-negative matrix factorization (NMF). The strong correlation observed between speckle components extracted from GM12878 Hi-C data and damage enrichment (Supplementary Fig. S4) further supports our interpretation that cisplatin-induced DNA damage is enriched in chromatin regions proximal to nuclear speckles.

Histone modifications and ChromHMM states are correlated with cisplatin-induced DNA damage through their nuclear positioning

To evaluate the impact of epigenetic modifications on cisplatin-induced DNA damage, we calculated the enrichment of histone modifications for EN and DP regions (Fig. 3K). Interestingly, H3K9me2—a "peripheral heterochromatin" marker [49]—is the only histone modification enriched in DP regions, consistent with our localization predictions and its enrichment in the silenced B3 subcompartment. As expected, all tested histone modifications related to transcriptional activation are elevated in EN and decreased at DP regions (Fig. 3K). However, EN regions are also enriched in repressive H3K27me3, which is associated with a silenced state and linked to polycomb repressed chromatin regions. We showed that B1 subcompartment chromatin, enriched in H3K27me3, preferentially localizes toward the nuclear interior, in proximity to nuclear speckles [23]. Additionally, polycomb bodies are known to be excluded from the nuclear periphery [28, 29]. These observations suggest that the interior locations of polycomb-repressed chromatin may contribute to its increased susceptibility to DNA damage, despite its silenced state.

We then studied if chromatin in different functional chromatin states show distinct enrichment of *in vivo* versus *in vitro* damage sites. To do this, we utilized the chromatin states annotated by ChromHMM [43], a software that integrates multiple epigenetic datasets to infer chromatin states through a multivariate hidden Markov model. As expected, DNA damage is slightly enriched in states associated with active chromatin, including promoters and enhancers, and slightly depleted at repressed chromatin, including heterochromatin and repetitive regions (Fig. 4A) [4]. However, when we stratify all genomic regions in each ChromHMM state into quintiles of their average radial positions, we found that cisplatin damage is again consistently enriched at inner nuclear positions, regardless of the ChromHMM states (Fig. 4A). The only exception is poised enhancers, which show neither enrichment nor depletion (Fig. 4A, chromatin state 3).

Active gene transcription and nuclear positioning correlate with DNA damage susceptibility

We further assessed the role of active gene transcription in cisplatin-induced damage enrichment. The majority of genes in EN regions are highly expressed, whereas genes in DP regions show lower expression levels (Fig. 4B). Consistently, Poll II ChIP-seq signals are enriched in EN and depleted in DP regions, with the strongest enrichment for Poll II Ser5p ChIP-seq data (elevated by ∼16%) (Supplementary Fig. S5) [50], linking

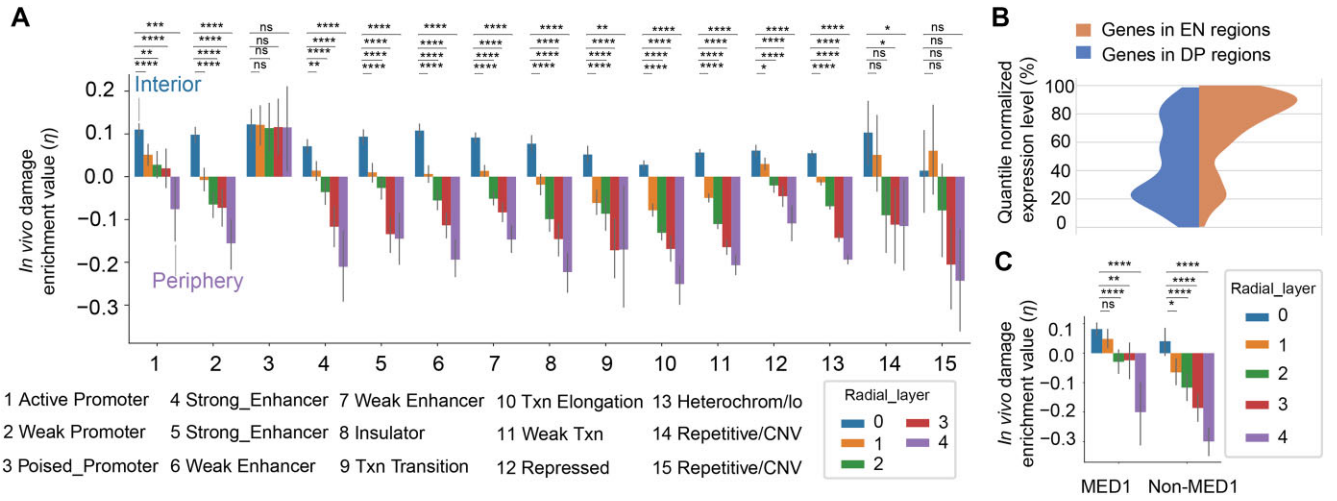

Figure 4. Active gene transcription and nuclear positioning both play a role in DNA damage susceptibility Individual chromatin states are detected by ChromHMM [40] and further stratified into radial position shells [within 0–0.2R (most interior), 0.2–0.4R, 0.4–0.6R, 0.6–0.8R, and 0.8–1R (most peripheral), with R representing the radius of nucleus]. (**A**) Median *in vivo* damage enrichment value for chromatin regions (at ∼1 kb resolution) stratified by their chromatin statesand radial positions. The chromatin states are represented by numbers and listed at right. Chromatin within the same ChromHMM state show highest damage enrichment toward the nuclear interior across all active and inactive chromatin states, with the exception of poised promoter chromatin, which shows the highest damage enrichment across all radial layers. Chromatin within the same ChromHMM state show highest damage enrichment toward the nuclear interior across all active and inactive chromatin states, error bar represent 95% CI (* p<0.05, ** p<0.01, *** p<0.001, **** p<0.0001). (**B**) Violin plot of gene expression levels in EN/DP regions. Gene expression level in GM12878 is downloaded from ENCODE and quantile normalized for all genes. Left half of violin plot show distribution of quantile normalized genes expression in DP regions. Right half of violin plot show distribution of quantile normalized genes expression in EN regions. *Y*-axis represent the quantile normalized gene expression level, e.g. 50% represent this fraction of gene have expression level higher than 50% of all genes. (**C**) Median *in vivo* damage enrichment value for chromatin regions stratified by their MED1 target states and radial positions. Non-MED1 targets are randomly picked from genome with same number and average length with MED1 targets, but at least 20 kb far away from MED1 targets (* p<0.05, ** p<0.01, *** p<0.001, **** p<0.0001).

elevated transcriptional activity to EN regions and enhanced cisplatin induced DNA damage.

A recent study revealed that cisplatin can be enriched in transcriptional condensates mediated by the MED1 subunit of the Mediator complex. MED1 also plays a particular role in super-enhancer organization and subsequent formation of active transcriptional hubs [51, 52]. Using a MED1 Chip-seq data [53] set, we found that *in vivo* damage enrichment values are significantly higher at sites bound by MED1 proteins in comparison to randomly selected non-MED1 target sites (non-MED1 sites were at least 20 kb away from MED1 ChIP-seq peaks). To investigate the influence of the radial position within MED1-binding sites, we then stratified MED-1 binding sites and non-MED1-binding sites into quintiles according to their average radial positions in our models. For both MED1 and non-MED1 target regions, cisplatin *in vivo* damage enrichment values were significantly higher toward the interior nuclear shells in comparison to regions located toward the nuclear periphery (Fig. 4C), thus emphasizing again the confounding role of the nuclear locations for DNA damage susceptibility even within regions under active transcription.

Chromatin accessibility is marginally correlated with cisplatin-induced DNA damage

We also tested if chromatin accessibility, rather than the nuclear locations, could explain the cisplatin damage patterns *in vivo*. We used ATAC-seq data as a measure for chromatin accessibility since this technology probes open chromatin regions at high resolution without requiring prior knowledge of regulatory elements [54]. Radial positions might impact both chromatin accessibility and *in vivo* damage enrichment. Open actively transcribed chromatin regions are generally located more toward the nuclear interior. We therefore remove the impact of radial positions, by computing the partial correlation between the *in vivo* DNA damage enrichment values of a genomic region and the ATAC-seq signal from experiment, conditioned by the radial position (Materials and methods). We observed a significant but relatively low partial correlation between *in vivo* DNA damage enrichment values and ATAC-seq signals (Spearman corr = 0.19, *P*-value∼0) (Fig. 5A). In contrast, when we computed the partial correlation between *in vivo* damage enrichment values of a genomic region and its radial position, conditioned by the ATAC-seq signals, we found a substantially higher partial correlation (Spearman corr = -0.67, *P*-value = 2.8×10^{-111}) (Fig. 5A). This result suggests that the nuclear location of a chromatin region is more closely related to the distribution of cisplatin damage than chromatin accessibility alone.

DNA repair does not correlate with cisplatin-induced DNA damage patterns

DNA repair can in principle affect the distribution of *in vivo* DNA damage. XR-seq is a sequencing-based technology that maps DNA nucleotide excision repair activity on a genome-wide scale [4]. We analyzed XR-seq data of GM12878 cells to assess the influence of DNA repair activity on DNA damage distributions. We found that XR-seq and cisplatin damage show highly correlated signal distributions (Fig. 5B, Spearman correlation = 0.65) (Fig. 5C). Moreover, chromatin regions with the top 10% XR-seq are concentrated in the nuclear interior and in close distances to nuclear speckles, coinciding the distribution of EN regions (Supplementary Fig. S6A). In

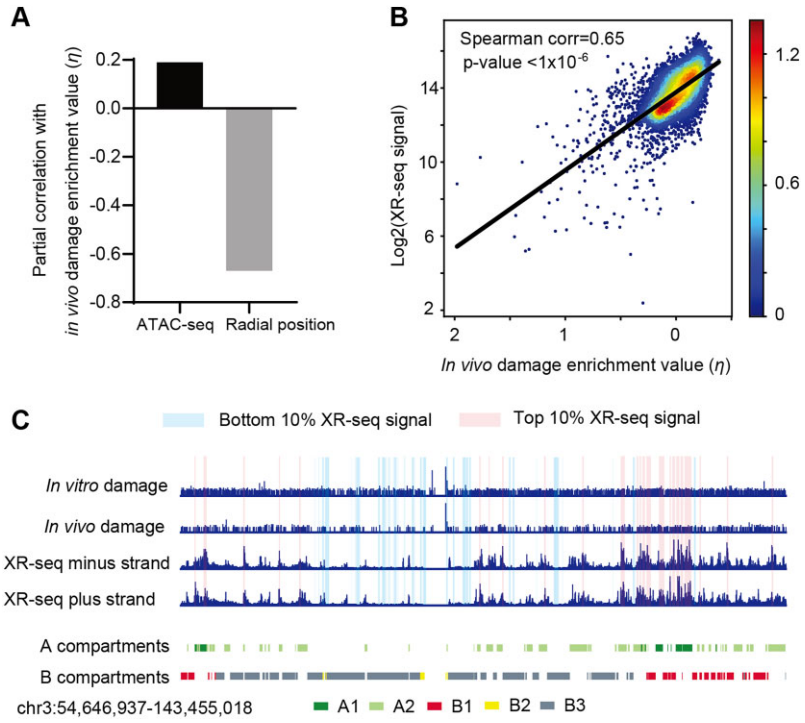

Figure 5. The role of chromatin accessibility and DNA damage repair on cisplatin damage enrichment. (**A**) Left bar: partial correlation between the *in vivo* damage enrichment value and ATAC-seq signals conditioning on average radial position for genomic regions at 200 kb resolution. Right bar: partial correlation between *in vivo* damage enrichment value and the average radial positions conditioning on ATAC-seq of genomic regions (Materials and methods). (**B**) Correlation between the XR-seq signals and *in vivo* damage enrichment value for all genomic regions (200 kb resolution). (**C**) Visualization of XR-seq signals, damage signals, and chromosome compartments in IGV for a 89 Mb region in chromosome 3; Highlighted blocks above the XR-seq tracks mark windows in the bottom 10% and top 10% XR-seq signal.

contrast, chromatin with the bottom 10% XR-seq signal does not have a clear preference in terms of nuclear positioning nor distances to nuclear speckles (Supplementary Fig. S6B).

It is well established that transcription-coupled repair (TCR) efficiently removes cisplatin-induced DNA damage, leading to higher XR-seq signals at actively transcribed genes [41, 55]. Since transcriptional activity is also generally higher in the nuclear interior, we aimed to disentangle whether the enrichment of XR-seq signals in the nuclear interior is driven by transcriptional activity or by nuclear positioning. To address this, we stratified genomic regions in GM12878 cells based on their transcriptional activity and further divided them according to the radial nuclear shell they occupy. Within each shell, XR-seq signals were consistently higher in highly expressed regions, confirming the known link between DNA nucleotide excision repair and transcriptional activity (Supplementary Fig. S7). However, when comparing XR-seq signals across shells, we found that moderately expressed regions in the inner nuclear shells (shells 1–6) had higher XR-seq signals than highly expressed regions in the outer nuclear shells (shells 8–10). This suggests that, while XR-seq signals correlate with transcriptional activity, they are also influenced by nuclear positioning, potentially due to higher levels of DNA damage in the nuclear interior.

Our observation suggests that the DNA repair does not fundamentally alter cisplatin-induced DNA damage patterns. Instead, the recruitment of DNA repair machinery likely occurs after the induction of DNA damage, resulting in the distribution of DNA repair activity mirroring the distribution of DNA damage.

Functional consequences of cisplatin-induced DNA damages

We further explored the type of genes that are most affected by cisplatin damage. Gene Ontology analysis shows that genes with elevated DNA damage levels (Fig. 6, left panel) are mainly involved in metabolic and cellular organelle organization processes, while genes with decreased damage levels (Fig. 6, right panel) are related to protein de-ubiquitination and immune response related pathways.

Overall, our findings indicate that the uneven distribution of cisplatin-induced DNA damage in the nucleus can perturb specific functional pathways, underscoring the interplay between nuclear organization and gene function.

The impact of nuclear positioning on Platinum-induced DNA damage in chemoresistant cancer cells

Finally, we explored the role of 3D nuclear architecture in chemoresistance to Platinum-based drugs in cancer, by analyzing genome structural differences between drug sensitive and drug-resistant HCT116 colon cancer cell lines. These cell lines have a near-diploid genome, facilitating genome structure modeling.

Oxaliplatin is a widely used platinum-based drug for colon cancer treatment. To investigate differences in the oxaliplatin-induced response, we focused on two HCT116 cell lines: the oxaliplatin-sensitive HCT116 OxS, (hereafter SEN) and the resistant HCT116 OxR (hereafter RES), which exhibits resistance to oxaliplatin treatment, with an IC_{50} of 7.21 μM compared to 0.59 μM in parental HCT116 cells [56]. We per-

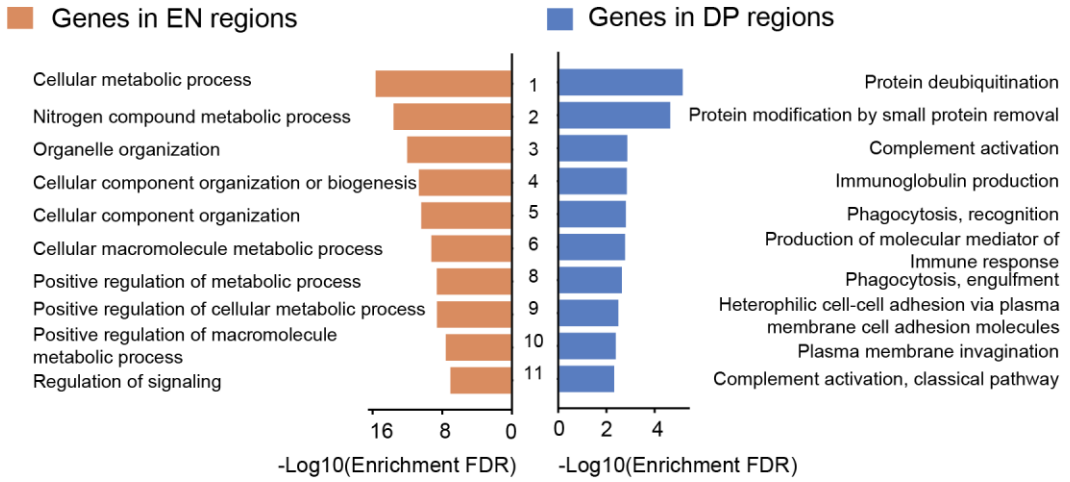

Figure 6. Downstream effect of the differentially damaged cisplatin regions(Left panel) Top 11 gene ontology groups for genes in EN regions with the highest damage enrichment FDR. (Right panel) Top 11 gene ontology groups for genes in DP regions with the highest damage enrichment FDR.

formed oxaliplatin DNA damage-seq on both cell lines (RES and SEN) under untreated and drug-treated conditions and Hi-C experiment on RES. Oxaliplatin has a higher cytotoxicity in colon cancer models [47] than cisplatin. To maintain consistency with cisplatin DNA damage-seq experiments, we selected a dose of oxaliplatin in HCT116 OxR cells that is ~10 times its IC_{50} value (i.e. 50 μM) [47].This choice ensures that DNA damage and cytotoxicity induced by oxaliplatin are comparable in magnitude to the effects observed in cisplatin-treated cells.

Following oxaliplatin administration, cells were incubated for 3 or 24 h to assess short- and long-term damage before quantifying the fold change in DNA damage between RES and SEN cells (Materials and methods). After 3 h of oxaliplatin treatment, we identified 449 chromatin regions with significant differences in DNA damage (FDR < 0.05). Among these, 122 regions showed increased DNA damage (fold change > 1), while 317 regions showed decreased DNA damage in RES cell (fold change < 1) (Supplementary Table S2) in comparison to SEN cells (Supplementary Fig. S8A).

A 24-h treatment significantly increased the number of chromatin regions (708 regions) with differential DNA damage between RES and SEN cells (FDR < 0.05). Of these, 226 regions showed significantly increased damage in RES cells, while 482 had significantly decreased damage (Supplementary Table S2 and Supplementary Fig. S8B). Overall, RES cells had almost twice as many regions with reduced than increased damage, supporting a global decrease in DNA damage in these cells. These findings are consistent with a previous study showing overall lower DNA damage levels in oxaliplatin-resistant compared to sensitive cell lines [57].

Following confirmation of the near-diploid status of RES cells (Materials and methods), we used IGM [22] to generate 3D genome structures of SEN and RES cells from Hi-C data without oxaliplatin treatment. We then analyzed the nuclear locations of regions with significantly altered DNA damage in RES cells. Regions with decreased damage were significantly closer to nuclear speckles and farther from the nuclear periphery in both SEN and RES cells after 3- and 24-h oxaliplatin treatments (Fig. 7 and Supplementary Fig. S9). In contrast, regions with increased damage in RES cells were closer to the lamina compartment at the nuclear periphery for both 3 h- (Supplementary Fig. S9B and D) and 24-h oxaliplatin treatments (Fig. 7B and D). However, the correlation between decreased DNA damage and higher speckle association is substantially stronger after 24 h of treatment (Fig. 7C and D) compared to 3 h (Supplementary Fig. S9C and D). Chromatin regions with high SAFs are enriched with housekeeping genes in gene-dense areas. In RES cells, regions with significantly decreased DNA damage are part of these gene-dense regions, while those with increased DNA damage are at the nuclear periphery in gene-poor regions (Fig. 8).

Discussion

Cisplatin and oxaliplatin are one of most widely used first-line anti-cancer drugs. Dissecting the cytotoxicity and mechanisms of resistance for Pt-drugs is key for improving their performance for chemotherapy. The essential events in the action of cisplatin include the entry and accumulation of cisplatin in the cytoplasm, the entry and spatial distribution of cisplatin in the nucleus, the crosslinking of DNA bases, and subsequent DNA repair activity. Unlike other extensively studied events, little research has been conducted on the uneven spatial distribution of cisplatin in the nucleus with potential consequences on cisplatin's action on DNA. The nucleus contains various phase-separated condensates that compartmentalize and potentially concentrate biomolecules based on their distinct physicochemical properties [14]. Recent evidence from *in vitro* experiments have shown that cisplatin could be enriched in biomolecular condensates linked to specific nuclear bodies and transcriptional condensates [14, 15], raising the possibility that the spatial distribution of cisplatin and subsequently the variation of its local concentration in the nuclear environment could play a key role in how effectively cisplatin can damage specific DNA regions. Moreover, it has been shown that a drug-response mechanism of cisplatin-treated cancer cells is the fragmentation and reduced sizes of nucleoli [16–18], which could potentially eradicate nuclear environments with high cisplatin concentrations. It is therefore of high significance to investigate if cisplatin-induced damage is increased at specific nuclear microenvironments, for instance locations of nuclear bodies in intact nuclei.

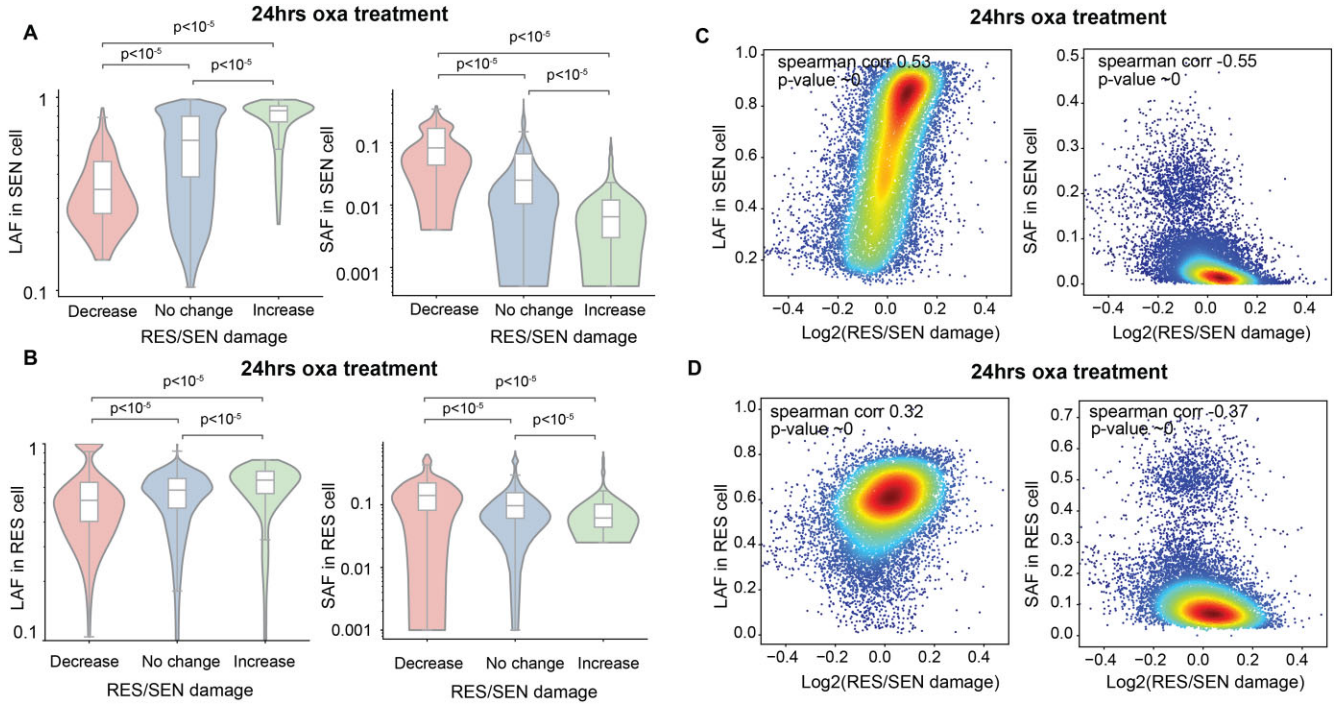

Figure 7. The impact of nuclear positioning on platinum-induced DNA damage in chemoresistant cancer cells (oxaliplatin treated 24 h) (**A**) Violinplot of (left panel) LAF and (right panel) SAF of genomic regions in SEN cell with significantly change of damage level in RES versus SEN cell treated by oxaliplatin for 24 h (damage decreased regions: *P*-adjust value < 0.05, fold change < 1, Damage increased regions: *P*-adjust value < 0.05, fold change > 1, other regions are without damage change) (**B**) Violinplot of (left panel) LAF and (right panel) SAF of genomic regions in RES cell with significantly change of damage level in RES versus SEN cell treated by oxaliplatin for 24 h (damage decreased regions: *P*-adjust value < 0.05, fold change < 1, damage increased regions: *P*-adjust value < 0.05, fold change > 1, other regions are without damage change) (**C**) Scatter plot of the (left panel) LAF and (right panel) SAF of each genomic region derived from the 3D genome structure population in SEN cell and its damage fold change in RES versus SEN cells, treated by oxaliplatin for 24 h. (**D**) Scatter plot of the (left panel) LAF and (right panel) SAF of each genomic region derived from the 3D genome structure population in RES cell and its damage fold change in RES versus SEN cells, treated by oxaliplatin for 24 h.

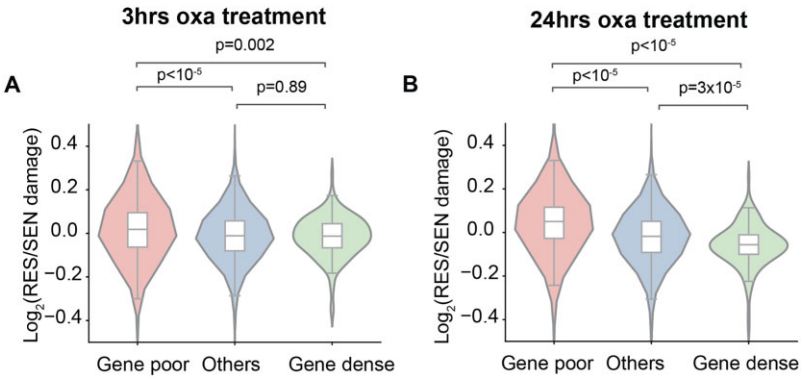

Figure 8. Damage level fold change in RES versus SEN cell at genomic regions with different gene density. (**A**) Violinplot of damage level fold change in RES versus SEN cell treated by oxaliplatin for 3 h at different genomic regions (gene dense regions: > 10 genes per 200 kb, gene poor regions: 0 genes per Mb, others: the rest of genomic regions). (**B**) Violinplot of damage level fold change in RES versus SEN cell treated by oxaliplatin for 24 h at different genomic regions (gene dense regions: >10 genes per 200 kb, Gene poor regions: 0 genes per Mb, others: the rest of genomic regions.

This study reveals that variations in cisplatin-induced DNA damage susceptibility across genomic regions correlates with their preferential spatial positioning within the 3D nuclear architecture. This suggests that the nuclear microenvironment can play a significant role in the distribution of cisplatin-induced DNA damage. We therefore explored the structural characteristics of the nuclear genome that contribute to the differential susceptibility of chromatin to DNA damage.

EN regions experience an increased likelihood of sustaining damage within the nuclear environment compared to isolated DNA. This observation suggests that genes containing EN regions are generally more prone to DNA damage compared to other genes, even at lower drug concentrations.

EN regions are generally enriched in the A compartment and depleted in B compartment, while DP regions are depleted in A compartment. However, cisplatin damage susceptibility can only partially be explained by the transcriptional status of the genes. Indeed, when stratifying chromatin based on Hi-C subcompartments, it is evident that EN regions are not only enriched in chromatin of the highly active A1 sub-

compartment, but also in chromatin in the silenced B1 subcompartment, which is associated with polycomb repressed chromatin regions, while EN regions are slightly depleted in chromatin of the transcriptionally active A2 subcompartment (Fig. 2B). This observation is confirmed by an enrichment of H3K27me3 in EN regions, which are known to be associated with polycomb silenced heterochromatin. Thus, increased DNA damage susceptibility *in vivo* cannot solely be explained by the transcriptional status of a gene alone.

We then explored the influence of the nuclear microenvironment on DNA damage susceptibility, by assessing the location of chromatin in the nucleus relative to nuclear bodies. This analysis was based on a population of 3D genome structures generated using Hi-C data through our population-based genome modeling approach [22, 23]. We made several interesting observations. The susceptibility to cisplatin DNA damage shows strong correlation with the nuclear locations of genomic regions, independent of the functional activity of genes. For chromatin in the transcriptionally active A compartment, we see a gradual increase in EN enrichment fold toward the interior of the nucleus. Similarly, B compartment chromatin shows the highest EN enrichment fold at the most interior radial shell. In contrast, DP regions show the opposite trend, with a strong DP enrichment toward the nuclear periphery. Our observations also find that silenced B1 subcompartment chromatin is enriched in EN regions, since it is preferentially located toward the nuclear interior, in contrast to lamina associated heterochromatin. Likewise, active A2 subcompartment chromatin, despite being transcriptionally active, does not show pronounced enrichment toward the nuclear interior and is not enriched in EN regions, (Fig. 2B). We confirmed our predictions with GPSeq experimental data (Supplementary Fig. S3) [24].

We found similar results using ChromHMM [43] to define chromatin functional states. Almost all ChromHMM states—including active promoters, active enhancers, and the heterochromatin—showed the highest damage fold enrichment at the most interior radial positions, with a gradual decrease of damage fold enrichment moving toward the outer radial locations (Fig. 4A).

Interestingly, we also found that the nuclear position of a chromatin region is a stronger indicator for *in vivo* cisplatin DNA damage enrichment than chromatin accessibility: the average radial position of a chromatin region shows a 3.5-fold higher partial correlation with DNA damage enrichment than chromatin accessibility measured in ATAC-seq experiments (Fig. 5A).

Although we find a clear dependency between interior nuclear positions and cisplatin DNA damage susceptibility, it is unknown what underlying factors could cause this correlation. Here, we showed that the distances to nuclear speckles can explain observed DNA damage susceptibility. Indeed, the correlation of *in vivo* damage enrichment values with speckle distances is higher than the correlation observed for radial positions (Fig. 3H). We further assessed these observations using TSA-seq data, which confirmed that EN regions are enriched with high SON TSA-seq signals [25], indicating smaller average speckle distances. Conversely, DP regions show depleted SON TSA-seq signals, consistent with larger speckle distances. Similarly, B1 subcompartment chromatin shows higher average SON TSA-seq signals, thus, smaller average nuclear speckle distances than transcriptionally active A2 chromatin [23], consistent with the observed higher *in vivo* DNA damage enrichment for B1 than for A2 chromatin.

This observation is interesting, because unlike radial positions, speckle distances could provide a physical rationale for increased DNA damage. It has been recently observed that cisplatin concentrations can be significantly increased in biomolecular condensates, including those in nuclear bodies [14, 15], indicating that proximities to high cisplatin concentrations in some nuclear bodies could explain increased cisplatin induced DNA damage in the nuclear environment.

Our findings rationalize an unusual observation; namely, that the nuclear microenvironment not only reduces DNA damage susceptibility for some chromatin regions in comparison to isolated DNA extracts but also can increase DNA damage susceptibility for other chromatin regions. While reduced DNA damage susceptibility can easily be rationalized by the protective nature of chromatin proteins, in particular for transcriptionally silenced and compact heterochromatin, the increased susceptibility of other regions is less comprehensible. Here, we show that increased DNA damage susceptibility within the nuclear environment is correlated with lower average distances to nuclear speckles. This observation could partially be explained by a potentially higher cisplatin concentration in condensates of specific nuclear bodies, as well as transcriptional biomolecular condensates.

Increased cisplatin-induced DNA damage susceptibility is likely a combination of several confounding factors, including contributions from chromatin accessibility, transcriptional activity, and local DNA repair efficiency. Here, we show that the location of genomic regions in the nucleus with respect to nuclear bodies play also a major role in DNA damage susceptibility. These findings should be considered when studying the molecular mechanisms of platinum-drug chemoresistance.

We also investigated the 3D nuclear distribution of DNA-damaged chromatin following oxaliplatin treatment in both drug-sensitive (SEN) and drug-resistant (RES) HCT116 cancer cells. Our analysis revealed that differences in DNA damage levels between SEN and RES cells are mapped to specific nuclear regions. For instance, in resistant cells, we observed reduced DNA damage in chromatin near nuclear speckles, coinciding with gene rich chromatin with highly active gene transcription, which could benefit cell survival by preserving essential gene functions. Conversely, RES cells show increased DNA damage accumulation in chromatin near the nuclear lamina compartment, a gene-poor region, where such damage may have a lesser impact on cell viability (Fig. 7). Thus, a more widespread nuclear distribution of oxaliplatin toward the nuclear periphery might help mitigate oxaliplatin-induced DNA damage on vital gene-dense chromatin regions located at the nuclear speckles, which often contain housekeeping genes crucial for cell survival. This observed spatial redistribution of DNA damage in cancer cells during the development of chemoresistance agrees with the classical "bodyguard hypothesis," which suggests that heterochromatin acts as a protective buffer, shielding gene rich euchromatin against DNA damage [58]. At this point, it remains unclear whether the redistribution of DNA damage in resistant cells contributes to resistance or is merely coincidental. Clarifying this relationship requires additional experiments across various resistant cell lines. It would be crucial to know whether this observed pattern of DNA damage represents an evolutionary adaptation to Platinum-based treatment, or merely a "survivorship

bias" among cancer cells during the selection of drug treatment. Other drug-resistant mechanisms, such as differences in the activity of membrane transporters, detoxification mechanisms, or DNA repair activity could be alternative adaptive strategies for cell survival. This discovery necessitates further investigations into how the nuclear architecture influences the development of chemoresistance.

Another promising avenue for future research is exploring how cisplatin-induced uneven DNA damage distribution within the nuclear architecture affects downstream physiological processes. This includes examining its effect on transcription, RNA splicing and overall gene expression regulation. Cisplatin-DNA adducts are well known to inhibit gene transcription through several mechanisms, including blocking RNA polymerase progression, obstructing transcription factor binding at promoter sites, and disrupting nucleosomal structure and mobility [59]. For instance, Merav *et al.* [60] compared gene expression in cisplatin-treated cells to untreated control and found a modest but highly significant negative correlation ($P = -0.36$, P-value: $<$ 2.2e-16) between gene expression fold change and the number of cisplatin-induced damage sites within a gene. This suggests that genes sustaining higher levels of damage experience greater transcriptional impairment. Additionally, their analysis showed that longer genes have significantly lower RNA-seq counts after cisplatin treatment, indicating they are more transcriptionally impaired than shorter genes, whose transcript levels are less affected [60]. We therefore expect genes with a higher number of EN regions to be more susceptible to transcriptional impairment. This study also demonstrated that at the dose of 200 μM cisplatin—the same concentration used in our analysis—leads to significant differences in cisplatin-induced transcriptional alterations across gene groups [60]. Despite the relatively high and potentially saturating dose of cisplatin, these findings highlight that even in the presence of extensive DNA damage, variations in damage levels among different genes remains functionally relevant. Moreover, given the connection between DNA damage susceptibility and genome architecture, we expect that differences in DNA damage susceptibility will persist even at lower drug doses.

Given these effects, it would be valuable to investigate whether genes located near nuclear speckles are more susceptible to transcriptional suppression due to elevated DNA damage levels on their gene bodies. Additionally, examining the downstream cellular and molecular effects, such as change of cell signaling, DNA repair, and apoptosis, that result from altered gene expression in these regions could provide critical insights into cisplatin's mode of action.

Cisplatin treatment may also disrupt RNA splicing by affecting SR splicing factors, potentially contributing to its cytotoxic effects [61]. Investigating how cisplatin-induced damage distribution influences RNA splicing in speckle-proximal genes could uncover novel mechanisms underlying its cellular impact and toxicity.

Notably, nuclear condensates, including speckles, are dynamic structures whose size, shape, and biophysical properties can evolve in response to platinum drug treatment. For example, studies have observed that certain speckle components, such as SR proteins, are redistributed to nucleoli following UV-induced DNA damage [62]. These findings suggest that DNA damage events may alter the protein and nucleic acid composition of nuclear speckles [61]. Such changes could further modulate the role of the nuclear architecture in DNA damage susceptibility. Future imaging studies could provide a deeper understanding of these dynamic changes by characterizing the protein and nucleic acid composition of nuclear bodies during cisplatin treatment. Such studies would enhance our understanding of how nuclear architecture mediates the distribution of DNA damage and its broader implications for cellular function and drug response.

Acknowledgements

We thank Charis Qi, Ryan Cope, Francesco Musella and Yuxiang Zhan for useful discussions. We also thanks Prof. Inkyung Jung for discussions on HiCAN software and for sharing of GM12878 HiCAN data.

Author contributions: Ye Wang (Conceptualization [lead], Data curation [lead], Formal analysis [lead], Writing—original draft [lead], Writing—review & editing [lead]), Asli Yildirim (Data curation [supporting], Resources [supporting], Software [supporting]), Lorenzo Boninsegna (Data curation [supporting], Resources [supporting], Software [supporting]), Valentina Christian (Validation [equal], Writing—review & editing [equal]), Sung-Hae L. Kang (Validation [equal], Writing—review & editing [equal]), Xianghong Jasmine Zhou (Conceptualization [equal], Funding acquisition [equal], Investigation [equal], Methodology [equal], Project administration [equal], Supervision [equal], Writing—original draft [equal], Writing—review & editing [equal]) and Frank Alber, (Conceptualization [equal], Funding acquisition [equal], Investigation [equal], Methodology [equal], Project administration [equal], Supervision [equal], Writing— original draft [equal], Writing—review & editing [equal])

Supplementary data

Supplementary data is available at NAR online.

Conflict of interest

Frank Alber is shareholder of EarlyDiagnostics Inc. in Agoura Hills, CA.

Xianghong Jasmine Zhou is co-founder and shareholder of EarlyDiagnostics Inc. in Agoura Hills, CA.

All other authors declare no conflicting interests.

Funding

This work was supported by the National Institutes of Health (grants UM1HG011593 to F.A; R01CA246329 to X.J.Z and U01CA285010 to X.J.Z. and F.A.). Funding to pay the Open Access publication charges for this article was provided by the National Institutes of Health.

Data availability

HCT116 OxR control cell Hi-C and Oxaliplatin damage-seq data generated by this paper are available in the GEO database under accession number GSE267578.

External experimental data source used in this study.

GM12878 Hi-C data was downloaded from 4DN data portal (https://data.4dnucleome.org/experiment-set-replicates/4DNES3JX38V5/).

HCT116 oxaliplatin sensitive cell (wild-type HCT116 without any treatment) Hi-C data were downloaded from 4DN data portal (https://data.4dnucleome.org/files-processed/4DNFIFLDVASC/).

The cisplatin damage-seq data of GM12878 cell were downloaded from (https://www.ncbi.nlm.nih.gov/geo/query/acc.cgi?acc=GSE82213).

GM12878 gene expression data were downloaded from ENCODE (https://www.encodeproject.org/experiments/ENCSR297UBP/).

ATAC-seq fold change signals (bigwig files) of GM12878 cells were downloaded from ENCODE (https://www.encodeproject.org/experiments/ENCSR095QNB/).

Histone modification data (except H3K9me2, bigwig files) for GM12878 were downloaded from ENCODE (https://www.encodeproject.org/search/?type=Experiment&control_type!=*&status=released&perturbed=false&assay_title=Histone±ChIP-seq&biosample_ontology.term_name=GM12878). There is no H3K9me2 data for GM12878 B lymphoblastoid cell so we downloaded the H3K9me2 data of human T cell data from https://dir.nhlbi.nih.gov/papers/lmi/epigenomes/hgtcell.aspx instead.

Pol II and Pol II Ser5p ChIP-seq data are downloaded from https://www.encodeproject.org/experiments/ENCSR000BGD/ and https://www.encodeproject.org/experiments/ENCSR000BIF/. MED1 ChIP-seq peaks is downloaded from GSE93080 [53] at GEO database.

There is no SON or Lamin B1 TSA-seq data of GM12878 cell so we downloaded the TSA-seq data of human immortalized myelogenous leukemia cell line K562 TSA-seq from 4DN data portal instead (bigwig files, https://data.4dnucleome.org/publications/0cbf34ae-fd3e-4b9d-a02f-cc80f1f8a872/#expsets-table).

The XR-seq data of GM12878 cell was downloaded from https://www.ncbi.nlm.nih.gov/geo/query/acc.cgi?acc=GSE82213 (bigwig files).

ChromHMM annotations were downloaded from UCSC (https://genome.ucsc.edu/cgi-bin/hgTrackUi?g=wgEncodeBroadHmm&db=hg19).

The 3D genome structure of GM12878 cell is from https://zenodo.org/records/7352276.

Code availability

The IGM source code, README file illustrating installation and execution, demo input, and expected outputs are all available at www.github.com/alberlab/igm/ and https://doi.org/10.5281/zenodo.15150846.

References

1. André T, Boni C, Mounedji-Boudiaf L *et al.* Oxaliplatin, fluorouracil, and leucovorin as adjuvant treatment for colon cancer. *N Engl J Med* 2004;**350**:2343–51. https://doi.org/10.1056/NEJMoa032709
2. Dasari S, Tchounwou PB. Cisplatin in cancer therapy: molecular mechanisms of action. *Eur J Pharmacol* 2014;**740**:364–78. https://doi.org/10.1016/j.ejphar.2014.07.025
3. Rottenberg S, Disler C, Perego P. The rediscovery of platinum-based cancer therapy. *Nat Rev Cancer* 2021;**21**:37–50. https://doi.org/10.1038/s41568-020-00308-y
4. Hu J, Lieb JD, Sancar A *et al.* Cisplatin DNA damage and repair maps of the human genome at single-nucleotide resolution. *Proc Natl Acad Sci USA* 2016;**113**:11507–12. https://doi.org/10.1073/pnas.1614430113
5. Shu X, Xiong X, Song J *et al.* Base-resolution analysis of cisplatin-DNA adducts at the genome scale. *Angew Chem Int Ed* 2016;**55**:14246–9. https://doi.org/10.1002/anie.201607380
6. Stenzel K, Hamacher A, Hansen FK *et al.* Alkoxyurea-based histone deacetylase inhibitors increase cisplatin potency in chemoresistant cancer cell lines. *J. Med. Chem.* 2017;**60**:5334–48. https://doi.org/10.1021/acs.jmedchem.6b01538
7. Eriksson M, Hååg P, Brzozowska B *et al.* Analysis of chromatin opening in heterochromatic non-small cell lung cancer tumor-initiating cells in relation to DNA-damaging antitumor treatment. *Int J Rad Oncol Biol Phys* 2018;**100**:174–87. https://doi.org/10.1016/j.ijrobp.2017.09.033
8. Zacharioudakis E, Agarwal P, Bartoli A *et al.* Chromatin regulates genome targeting with cisplatin. *Angew Chem Int Ed* 2017;**56**:6483–7. https://doi.org/10.1002/anie.201701144
9. Pflieger M, Hamacher A, Öz T *et al.* Novel α, β-unsaturated hydroxamic acid derivatives overcome cisplatin resistance. *Bioorg Med Chem* 2019;**27**:115036. https://doi.org/10.1016/j.bmc.2019.07.052
10. Fischer C, Leithner K, Wohlkoenig C *et al.* Panobinostat reduces hypoxia-induced cisplatin resistance of non-small cell lung carcinoma cells via HIF-1α destabilization. *Mol Cancer* 2015;**14**:4. https://doi.org/10.1186/1476-4598-14-4
11. Wang G, Edwards H, Caldwell JT *et al.* Panobinostat synergistically enhances the cytotoxic effects of cisplatin, doxorubicin or etoposide on high-risk neuroblastoma cells. *PLoS One* 2013;**8**:e76662. https://doi.org/10.1371/journal.pone.0076662
12. Sun Y, Bao X, Ren Y *et al.* Targeting HDAC/OAZ1 axis with a novel inhibitor effectively reverses cisplatin resistance in non-small cell lung cancer. *Cell Death Dis* 2019;**10**:400. https://doi.org/10.1038/s41419-019-1597-y
13. Han C, Srivastava AK, Cui T *et al.* Differential DNA lesion formation and repair in heterochromatin and euchromatin. *CARCIN* 2016;**37**:129–38. https://doi.org/10.1093/carcin/bgv247
14. Klein IA, Boija A, Afeyan LK *et al.* Partitioning of cancer therapeutics in nuclear condensates. *Science* 2020;**368**:1386–92. https://doi.org/10.1126/science.aaz4427
15. Rovira-Clavé X, Jiang S, Bai Y *et al.* Subcellular localization of biomolecules and drug distribution by high-definition ion beam imaging. *Nat Commun* 2021;**12**:4628. https://doi.org/10.1038/s41467-021-24822-1
16. Horky M, Wurzer G, Kotala V *et al.* Segregation of nucleolar components coincides with caspase-3 activation in cisplatin-treated HeLa cells. *J Cell Sci* 2001;**114**:663–70. https://doi.org/10.1242/jcs.114.4.663
17. Schmidt HB, Jaafar ZA, Wulff BE *et al.* Oxaliplatin disrupts nucleolar function through biophysical disintegration. *Cell Rep* 2022;**41**:111629. https://doi.org/10.1016/j.celrep.2022.111629
18. Sutton EC, DeRose VJ. Early nucleolar responses differentiate mechanisms of cell death induced by oxaliplatin and cisplatin. *J Biol Chem* 2021;**296**:100633. https://doi.org/10.1016/j.jbc.2021.100633
19. Misteli T. The self-organizing genome: principles of genome architecture and function. *Cell* 2020;**183**:28–45. https://doi.org/10.1016/j.cell.2020.09.014
20. Belmont AS. Nuclear compartments: an incomplete primer to nuclear compartments, bodies, and genome organization relative to nuclear architecture. *Cold Spring Harb Perspect Biol* 2022;**14**:a041268. https://doi.org/10.1101/cshperspect.a041268

21. Hua N, Tjong H, Shin H *et al.* Producing genome structure populations with the dynamic and automated PGS software. *Nat Protoc* 2018;**13**:915–26. https://doi.org/10.1038/nprot.2018.008
22. Boninsegna L, Yildirim A, Polles G *et al.* Integrative genome modeling platform reveals essentiality of rare contact events in 3D genome organizations. *Nat Methods* 2022;**19**:938–49. https://doi.org/10.1038/s41592-022-01527-x
23. Yildirim A, Hua N, Boninsegna L *et al.* Evaluating the role of the nuclear microenvironment in gene function by population-based modeling. *Nat Struct Mol Biol* 2023;**30**:1193–206. https://doi.org/10.1038/s41594-023-01036-1
24. Girelli G, Custodio J, Kallas T *et al.* GPSeq reveals the radial organization of chromatin in the cell nucleus. *Nat Biotechnol* 2020;**38**:1184–93. https://doi.org/10.1038/s41587-020-0519-y
25. Chen Y, Zhang Y, Wang Y *et al.* Mapping 3D genome organization relative to nuclear compartments using TSA-Seq as a cytological ruler. *J Cell Biol* 2018;**217**:4025–48. https://doi.org/10.1083/jcb.201807108
26. van Schaik T, Vos M, Peric-Hupkes D *et al.* Cell cycle dynamics of lamina-associated DNA. *EMBO Rep* 2020;**21**:e50636. https://doi.org/10.15252/embr.202050636
27. Su J-H, Zheng P, Kinrot SS *et al.* Genome-scale imaging of the 3D organization and transcriptional activity of chromatin. *Cell* 2020;**182**:1641–59. https://doi.org/10.1016/j.cell.2020.07.032
28. Cesarini E, Mozzetta C, Marullo F *et al.* Lamin A/C sustains PcG protein architecture, maintaining transcriptional repression at target genes. *J Cell Biol* 2015;**211**:533–51. https://doi.org/10.1083/jcb.201504035
29. Marullo F, Cesarini E, Antonelli L *et al.* Nucleoplasmic lamin A/C and Polycomb group of proteins: an evolutionarily conserved interplay. *Nucleus* 2016;**7**:103–11. https://doi.org/10.1080/19491034.2016.1157675
30. Hsu TC. A possible function of constitutive heterochromatin: the bodyguard hyp othesis. *Genetics* 1975;**79**:137–50.
31. Abdel-Rahman WM, Katsura K, Rens W *et al.* Spectral karyotyping suggests additional subsets of colorectal cancers characterized by pattern of chromosome rearrangement. *Proc. Natl. Acad. Sci. USA* 2001;**98**:2538–43. https://doi.org/10.1073/pnas.041603298
32. Masramon L, Ribas M, Cifuentes P *et al.* Cytogenetic characterization of two colon cell lines by using conventional g-banding, comparative genomic hybridization, and whole chromosome painting. *Cancer Genet Cytogenet* 2000;**121**:17–21. https://doi.org/10.1016/S0165-4608(00)00219-3
33. Hu J, Adebali O, Adar S *et al.* Dynamic maps of UV damage formation and repair for the human genome. *Proc Natl Acad Sci USA* 2017;**114**:6758–63. https://doi.org/10.1073/pnas.1706522114
34. Rao SSP, Huang S-C, St Hilaire G *et al.* Cohesin loss eliminates all loop domains. *Cell* 2017;**171**:305–20. https://doi.org/10.1016/j.cell.2017.09.026
35. Tjong H, Li W, Kalhor R *et al.* Population-based 3D genome structure analysis reveals driving forces in spatial genome organization. *Proc Natl Acad Sci USA* 2016;**113**:E1663–72. https://doi.org/10.1073/pnas.1512577113
36. Enright AJ, Van Dongen S, Ouzounis CA. An efficient algorithm for large-scale detection of protein families. *Nucleic Acids Res* 2002;**30**:1575–84. https://doi.org/10.1093/nar/30.7.1575
37. Németh A, Conesa A, Santoyo-Lopez J *et al.* Initial genomics of the human nucleolus. *PLoS Genet* 2010;**6**:e1000889. https://doi.org/10.1371/journal.pgen.1000889
38. Bolger AM, Lohse M, Usadel B. Trimmomatic: a flexible trimmer for Illumina sequence data. *Bioinformatics* 2014;**30**:2114–20. https://doi.org/10.1093/bioinformatics/btu170
39. Kim D, Langmead B, Salzberg SL. HISAT: a fast spliced aligner with low memory requirements. *Nat Methods* 2015;**12**:357–60. https://doi.org/10.1038/nmeth.3317
40. Li H, Handsaker B, Wysoker A *et al.* The Sequence Alignment/Map format and SAMtools. *Bioinformatics* 2009;**25**:2078–9. https://doi.org/10.1093/bioinformatics/btp352
41. Yimit A, Adebali O, Sancar A *et al.* Differential damage and repair of DNA-adducts induced by anti-cancer drug cisplatin across mouse organs. *Nat Commun* 2019;**10**:309. https://doi.org/10.1038/s41467-019-08290-2
42. Love MI, Huber W, Anders S. Moderated estimation of fold change and dispersion for RNA-seq data with DESeq2. *Genome Biol* 2014;**15**:550. https://doi.org/10.1186/s13059-014-0550-8
43. Ernst J, Kellis M. ChromHMM: automating chromatin-state discovery and characterization. *Nat Methods* 2012;**9**:215–6. https://doi.org/10.1038/nmeth.1906
44. Rao SSP, Huntley MH, Durand NC *et al.* A 3D map of the human genome at kilobase resolution reveals principles of chromatin looping. *Cell* 2014;**159**:1665–80. https://doi.org/10.1016/j.cell.2014.11.021
45. de la Fuente A, Bing N, Hoeschele I *et al.* Discovery of meaningful associations in genomic data using partial correlation coefficients. *Bioinformatics* 2004;**20**:3565–74. https://doi.org/10.1093/bioinformatics/bth445
46. Hu J, Lieb JD, Sancar A *et al.* Cisplatin DNA damage and repair maps of the human genome at single-nuc leotide resolution. *Proc Natl Acad Sci USA* 2016;**113**:11507–12. https://doi.org/10.1073/pnas.1614430113
47. Yang W, Soares J, Greninger P *et al.* Genomics of Drug Sensitivity in Cancer (GDSC): a resource for therapeutic biomarker discovery in cancer cells. *Nucleic Acids Res* 2013;**41**:D955–61. https://doi.org/10.1093/nar/gks1111
48. Lieberman-Aiden E, van Berkum NL, Williams L *et al.* Comprehensive mapping of long-range interactions reveals folding principles of the human genome. *Science* 2009;**326**:289–93. https://doi.org/10.1126/science.1181369
49. Poleshko A, Smith CL, Nguyen SC *et al.* H3K9me2 orchestrates inheritance of spatial positioning of peripheral heterochromatin through mitosis. *eLife* 2019;**8**:e49278. https://doi.org/10.7554/eLife.49278
50. Phatnani HP, Greenleaf AL. Phosphorylation and functions of the RNA polymerase II CTD. *Genes Dev.* 2006;**20**:2922–36. https://doi.org/10.1101/gad.1477006
51. Whyte WA, Orlando DA, Hnisz D *et al.* Master transcription factors and mediator establish super-enhancers at key cell identity genes. *Cell* 2013;**153**:307–19. https://doi.org/10.1016/j.cell.2013.03.035
52. Lovén J, Hoke HA, Lin CY *et al.* Selective inhibition of tumor oncogenes by disruption of super-enhancers. *Cell* 2013;**153**:320–34. https://doi.org/10.1016/j.cell.2013.03.036
53. Boudaoud I, Fournier É, Baguette A *et al.* Connected gene communities underlie transcriptional changes in cornelia de lange syndrome. *Genetics* 2017;**207**:139–51. https://doi.org/10.1534/genetics.117.202291
54. Buenrostro JD, Giresi PG, Zaba LC *et al.* Transposition of native chromatin for fast and sensitive epigenomic profiling of open chromatin, DNA-binding proteins and nucleosome position. *Nat Methods* 2013;**10**:1213–8. https://doi.org/10.1038/nmeth.2688
55. Adar S, Hu J, Lieb JD *et al.* Genome-wide kinetics of DNA excision repair in relation to chromatin state and mutagenesis. *Proc Natl Acad Sci USA* 2016;**113**:E2124–33. https://doi.org/10.1073/pnas.1603388113
56. Greenlee JD, Lopez-Cavestany M, Ortiz-Otero N *et al.* Oxaliplatin resistance in colorectal cancer enhances TRAIL sensitivity via death receptor 4 upregulation and lipid raft localization. *eLife* 2021;**10**:e67750. https://doi.org/10.7554/eLife.67750
57. Vaughn CM, Selby CP, Yang Y *et al.* Genome-wide single-nucleotide resolution of oxaliplatin-DNA adduct repair in drug-sensitive and -resistant colorectal cancer cell lines. *J Biol Chem* 2020;**295**:7584–94. https://doi.org/10.1074/jbc.RA120.013347

58. Hsu TC. A possible function of constitutive heterochromatin: the bodyguard hypothesis. *Genetics* 1975;**79**:137–50.
59. Todd RC, Lippard SJ. Inhibition of transcription by platinum antitumor compounds. *Metallomics* 2009;**1**:280–91. https://doi.org/10.1039/b907567d
60. Merav M, Bitensky EM, Heilbrun EE *et al.* Gene architecture is a determinant of the transcriptional response to bulky DNA damages. *Life Sci. Alliance* 2024;**7**:e202302328. https://doi.org/10.26508/lsa.202302328
61. Gabriel M, Delforge Y, Deward A *et al.* Role of the splicing factor SRSF4 in cisplatin-induced modifications of pre-mRNA splicing and apoptosis. *BMC Cancer* 2015;**15**:227. https://doi.org/10.1186/s12885-015-1259-0
62. Sakashita E, Endo H. SR and SR-related proteins redistribute to segregated fibrillar compon ents of nucleoli in a response to DNA damage. *Nucleus* 2010;**1**:367–80. https://doi.org/10.4161/nucl.1.4.12683

Received: June 25, 2024. **Revised:** March 31, 2025. **Editorial Decision:** April 1, 2025. **Accepted:** May 23, 2025